A continual learning-based multilayer perceptron for improved reconstruction of three-dimensional nitrate concentration

Xiang Yu[a,b], Huadong Guo[b], Jiahua Zhang[a,b], Yi Ma[c], Xiaopeng Wang[a], Guangsheng Liu[a], Mingming Xing[b], Nuo Xu[d], and Ayalkibet M. Seka[a,b,e]

[a]Remote Sensing Information and Digital Earth Center, College of Computer Science and Technology, Qingdao University, Qingdao, 266071, China
[b]Aerospace Information Research Institute, Chinese Academy of Sciences, Beijing, 100094, China
[c]First Institute of Oceanography Ministry of National Resource, Qingdao, 266061, China
[d]Department of Biological and Agricultural Engineering, University of California, Davis, 95616, USA
[e]Arba Minch Water Technology Institute, Water Resources Research Center, Arba Minch University, Ethiopia

Correspondence: Jiahua Zhang (zhangjh@radi.ac.cn)

Abstract. Nitrate plays a crucial role in marine ecosystems, as it influences primary productivity. Despite its ecological significance, accurately mapping its three-dimensional (3D) concentration on a large scale remains a considerable challenge due to the inherent limitations of existing methodologies. To address this issue, this study proposes a continual learning-based multilayer perceptron (MLP) model to reconstruct the 3D ocean nitrate concentrations above 2000 m depth over the pan-European coast. The continual learning strategy enhances the model generalization by integrating knowledge from Copernicus Marine Environmental Monitoring Service (CMEMS) nitrate data, effectively overcoming the spatial limitations of BGC-Argo observations in comprehensive nitrate characterization. The proposed approach integrates the advantages of extensive spatial remote sensing observations, the precision of Biogeochemical Argo (BGC-Argo) measurements, and the broad knowledge from simulated nitrate datasets, exploiting the capacity of neural networks to model their nonlinear relationships between multi-source sea surface environmental variables and subsurface nitrates. The model achieves excellent performance in profile cross-validation ($R^2 = 0.98$, RMSE=0.592 $\mu mol \cdot kg^{-1}$), and maintains robustness across diverse 3D validation scenarios, suggesting its effectiveness in filling observational gaps and reconstructing the 3D nitrate field. Then, the spatiotemporal distribution of the reconstructed 3D nitrate field from 2010 to 2023 reveals a spatial distribution pattern, an interannual upward trend, and the degree of consistency in vertical variation. The contributions of all 22 input features to the model's estimation were respectively quantified by using Shapley additive explanations values. This study reveals the potential of the proposed approach to overcoming observational limitations and enrich further insights into the 3D ocean condition. The reconstructed 3D nitrate dataset is freely available at https://doi.org/10.5281/zenodo.14010813 (Yu et al., 2024).

1 Introduction

In the last decade, the global oceans have absorbed approximately 25% of anthropogenic carbon dioxide (CO_2) from the atmosphere, playing a crucial role in mitigating climate change impacts (Friedlingstein et al., 2020). However, oceanic changes, such as warming and eutrophication may alter this role, leading to complex effects on marine ecosystems and climate. As the

primary limiting nutrient in the upper ocean, nitrate is pivotal in regulating primary productivity, especially new productivity (Bristow et al., 2017; Chen et al., 2023). This could constitute a long-term absorption of CO2 from the surface to the ocean interior (Eppley and Peterson, 1979; Gregg et al., 2003; Joo et al., 2016; Rafter et al., 2017). Thus, a comprehensive comprehension of the temporal and spatial distribution of ocean nitrate is indispensable for conducting research on marine ecology and environment.

Most biogeochemical data are collected in situ via coastal surveillance, oceanographic cruises, offshore platforms or autonomous instruments, such as the Global Ocean Data Analysis Project version 2 database (GLODAPv2) and Biogeochemical Argo (BGC-Argo) (Claustre et al., 2020; Lavigne et al., 2015; Nittis et al., 2007). However, traditional in situ measurements alone cannot provide large-scale and continuous nitrate data. In contrast, remote sensing offers a promising alternative for estimating nitrate due to its broad spatial coverage, temporal consistency, and cost-effectiveness (Chang et al., 2013; Pan et al., 2018). Previous research has successfully utilized it to retrieve water nutrients (Ansper and Alikas, 2019; Du et al., 2020; Mortula et al., 2020; Yu et al., 2016). Machine learning (ML) technologies have also been employed for nutrient concentration retrieval (Huang et al., 2021; Lv et al., 2020; Qun'ou et al., 2021).

Optical satellites face challenges in nitrate retrieval due to the lack of distinctive nitrate signals(Chen et al., 2023; Sathyendranath et al., 1991). Previous studies have demonstrated a strong empirical correlation between sea surface nitrate (SSN) and certain measurable seawater parameters (Goes et al., 2000; Joo et al., 2018; Kamykowski et al., 2002; Silió-Calzada et al., 2008; Switzer et al., 2003). Physical processes, biological activity, and chemical reactions like nitrification are commonly recognized as the three principal processes in regulating ocean nitrate (Goes et al., 2000, 1999; Kudela and Dugdale, 2000; Pan et al., 2018). Cold and nitrate-rich water is transported to the euphotic layer through physical processes, including upwelling and convective mixing in winter, enriching SSN while decreasing sea surface temperature (SST) (Kudela and Dugdale, 2000; Pan et al., 2018). Phytoplankton growth consumes nitrate and converts it into organic matter, reducing SSN while increasing Chlorophyll concentration (Chl) (Goes et al., 2000, 1999). Therefore, various physical and biogeochemical characteristics were frequently utilized as features to establish empirical connections with SSN. The conventional method for nitrate retrieval typically relies solely on SST for linear regression, given its negative relationship with SSN (Sarangi and Devi, 2017; Switzer et al., 2003). Nevertheless, the correlation between SST and SSN is subject to significant geographical and temporal variation, influenced by differing environmental conditions across regions (Goes et al., 1999; Silió-Calzada et al., 2008). Goes et al. (1999) found that incorporating Chl-a alongside SST notably improves the accuracy of SSN retrieval compared to using SST in isolation. Additionally, Colored dissolved organic matter (CDOM) is also a feasible candidate for oceans with considerable river inflow (Pan et al., 2018).

One primary limitation of remote sensing retrieval is the challenge of accurately monitoring subsurface environmental parameters (Akbari et al., 2017; Ali et al., 2004). While in situ data provide precise measurements of local vertical conditions, they are inadequate in characterizing ecosystem processes occurring at the extensive temporal and spatial scales involved (Von Schuckmann et al., 2019). Accurate 3D data acquisition for key variables over extensive scales is necessary for a deeper understanding of marine ecosystems (Rossi et al., 2021). To address this issue, various methods including modeling ecosystems and ocean dynamics have been explored to estimate biogeochemical variables, with some being widely applied (Baretta

et al., 1995; Bruggeman and Bolding, 2014; Holt et al., 2012; Kay and Butenschön, 2018). However, these methods require a thorough representation of physical and biological processes with highly nonlinear dynamics. While they can simulate environmental parameters and their distribution mechanisms, they may not always achieve the accuracy needed for specific applications (Storto et al., 2019; Tian et al., 2022).

In contrast, synergizing the extensive coverage of satellite data with the high precision of in situ data represents an effective approach, enabling the frequent characterization of the ocean's vertical structure across an expanded spatial scope (Buongiorno Nardelli, 2020; Tian et al., 2022; Gao et al., 2024; Zhou and Zhang, 2023). Empirical models were widely used to extrapolate important ocean variables from the surface to deeper layers (Morel and Berthon, 1989; Uitz et al., 2006), but they were vulnerable to inaccurate estimates due to the intricacy and non-linearity, particularly in locations with irregular vertical stratification and small-scale phenomena (Sammartino et al., 2020). Recent advancements in neural network (NN) technology have yielded promising results in addressing this issue (Asdar et al., 2024). For instance, Richardson et al. (2002) pioneered the use of an unsupervised NN for vertical chlorophyll reconstruction. Supervised NNs are capable of fitting nonlinear relationships between sea surface environmental variables and deep-sea conditions and have been successfully applied to the estimation or prediction of various subsurface ocean parameters such as temperature and salinity (Buongiorno Nardelli, 2020; Qi et al., 2022; Smith et al., 2023; Su et al., 2021), and density (Su et al., 2024). Additional studies have supplemented sea surface parameters with reanalysis or profile data to reconstruct more subsurface parameters (Hu et al., 2023; Tian et al., 2022; Zhou and Zhang, 2023). However, due to the complex mechanisms and heterogeneous distribution of nitrate (Webb, 2021), its 3D reconstruction was not developed as effectively as parameters like temperature, particularly as the need for concurrent vertical observations of additional variables persists. Wang et al. (2023) employed a regionalized deep neural network (DNN) to estimate nitrate concentration in the northwestern Pacific Ocean. Similar supervised techniques based on the Multilayer Perceptron (MLP) have been utilized to rebuild water-column bio-optical and biogeochemical variables using remote sensing and BCG-Argo data (Fourrier et al., 2020; Sauzède et al., 2017). A Bayesian strategy was proposed to supplement in situ data by inferring vertical profiles of unmeasured variables (Bittig et al., 2018). Yang et al. (2024) successfully reconstructed the 3D nitrate structure of the Indian Ocean from surface data using two advanced artificial intelligence networks. However, relying on simulated data rather than actual observations for training cannot overcome the its inherent uncertainties, which may limit the model's applicability in real ocean environments.

In this study, we develop an MLP to accurately reconstruct the 3D nitrate concentration upper 2000 m ocean, addressing the aforementioned challenges. Including vertical profile variables among the features might introduce potential uncertainty and limit the expansion of the estimation range, so input features are exclusively based on sea surface environmental variables. The model employs a continual learning strategy (Kirkpatrick et al., 2017), initially pre-training on simulated nitrate data to boost its generalization capabilities. The 3D nitrate field of the pan-European ocean from 2010 to 2023 is reconstructed based on this model and reveals the spatiotemporal distribution and interannual variations. Additionally, the contribution of each feature to the model estimates is calculated using Shapley values (Lundberg and Lee, 2017; Shapley, 1988), quantifying the effectiveness of features.

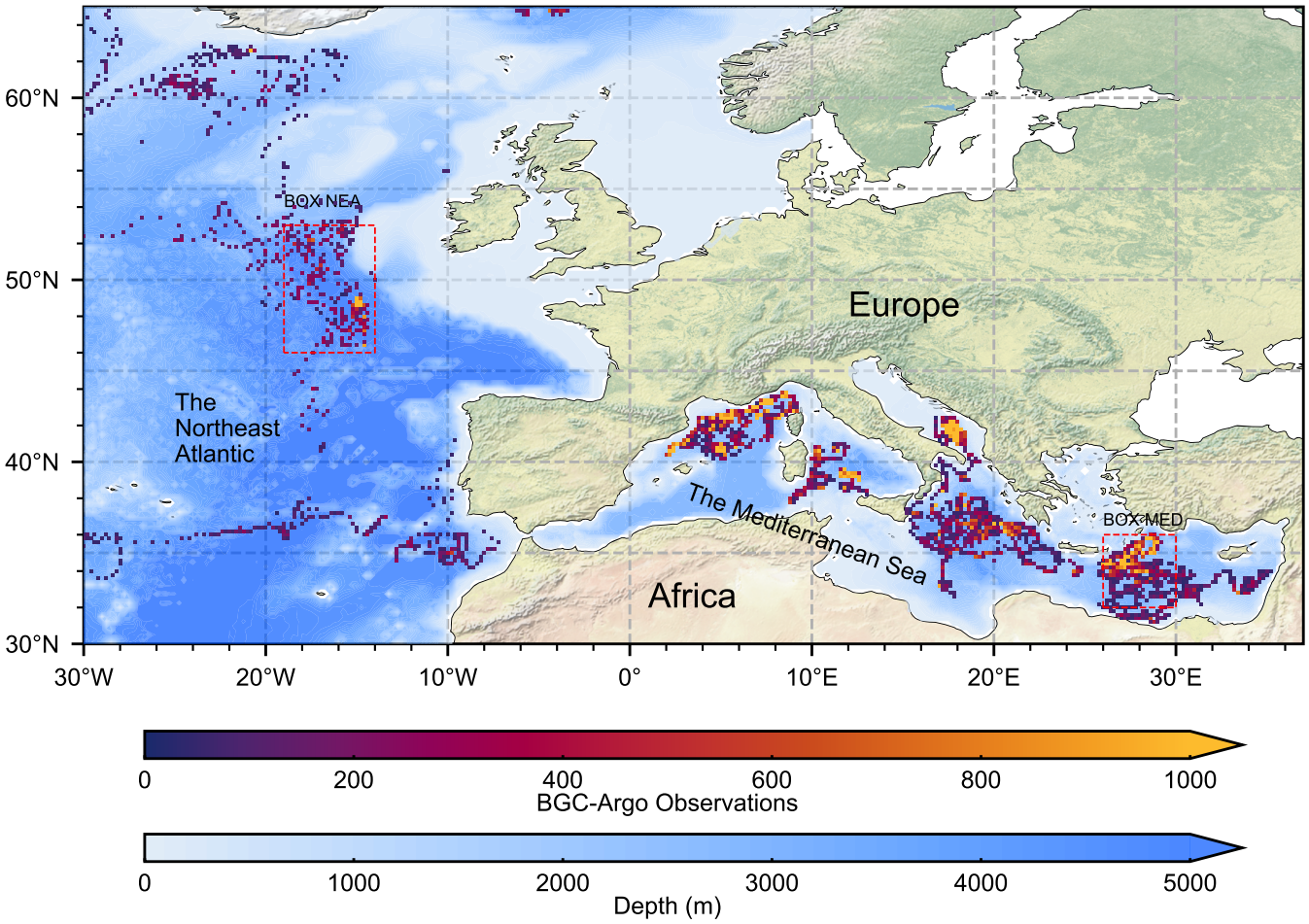

Figure 1. The pan-European domain, including the MED and the NEA. The study area is highlighted in blue, with shades of color indicating ocean depth. The warm-colored grid indicates the count of BGC-Argo observations. Two rectangular boxes are selected as typical data regions for pattern comparison.

2 Material and methods

2.1 Study area

The study area extends from 30° W to 37° E latitude and 30° N to 65° N longitude, covering the Mediterranean Sea (MED) and a portion of the Northeast Atlantic (NEA). This area is considered to be coastal of the pan-European domain, as shown in Fig. 1. It represents a critical zone for biogeochemical studies due to its extensive BGC-Argo observations and its unique position as one of the most data-rich coastal-proximate areas, where a portion of the continental shelf seas within this domain exhibit disproportionately high primary productivity and play a fundamental role in regulating oceanic biogeochemical cycles (Longhurst et al., 1995; Holt et al., 2009; Smith and Hollibaugh, 1993).

Nutrients from the open ocean and river runoff create a general and rapid biogeochemical cycle in the NEA (Gattuso et al., 1998), in contrast to the MED, which is distinguished for its semi-enclosure and oligotrophy conditions. This study aims to validate its effectiveness in different marine regions by exploring the relationships among multiple variables and developing a robust and generalizable modeling framework.

2.2 Data

2.2.1 In situ nitrate data

The in situ data of nitrate concentration used in this study were obtained through BGC-Argo (https://argo.ucsd.edu, https://www.ocean-ops.org), a network of profiling floats equipped with sensors capable of monitoring six biogeochemical variables (Claustre et al., 2020). The time, longitude, latitude, and pressure representing the depth are also recorded during the observations. Nitrate concentration is measured using ultraviolet absorption spectroscopy (Johnson et al., 2024), with an average accuracy of $\pm 0.5 \mu mol \cdot kg^{-1}$ (Johnson et al., 2021, 2017; Mignot et al., 2019). In this study, a total of 477,870 data in the study area are used, with 409,011 collected from the MED and 68,859 from the NEA.

The GLODAPv2 Database (https://doi.org/10.25921/1f4w-0t92) provides a uniformly calibrated open ocean data product on inorganic carbon and carbon-relevant variables (Lauvset et al., 2022, 2021; Olsen et al., 2020). GLODAPv2 contains 15 cruises within the study area, utilized for independent validation of the model's predictive performance.

2.2.2 Simulated nitrate data

While the BGC-Argo network provides a significant amount of in situ data on nitrate concentration, its spatial coverage remains inadequate for the entirety of the ocean. Notably, BGC-Argo deployments are sparse in the NEA and coastal areas, where nitrate concentrations are higher and of greater environmental concern (Berglund et al., 2023; Moore et al., 2013). Conventional deep learning algorithms typically only perform well when there is a high similarity between test and training datasets. The lack of comprehensive in situ observations can introduce bias into the training dataset, adversely affecting the performance and generalization ability of the model. Hence, integrating BGC-Argo nitrate observations with broad simulated nitrate data becomes crucial.

Simulated nitrate data is obtained from The CMEMS. The GLOBAL_MULTIYEAR_BGC_001_029 (https://doi.org/10.48670/moi-00019) product provides daily and monthly analyses of biogeochemical variables with a horizontal resolution of 0.25°×0.25° and feature 75 vertical levels. These products are based on the Pelagic Interactions Scheme for Carbon and Ecosystem Studies (PISCES) biogeochemical model (Aumont et al., 2015), which is part of the Nucleus for European Modelling of the Ocean (NEMO) modeling platform (Madec, 2016). The model can simulate biogeochemical cycles across various oceanic provinces and has been successfully employed in various biogeochemical studies (Tian et al., 2022; Yang et al., 2024).

2.2.3 Matching sea surface environmental variables datasets

Sea surface environmental variables (SSEV) matched to in situ nitrate data are used as input features for the model, detailed in Table 1. The SSEV data all span from 2010 to 2023, matching the BGC-Argo data since 2012 and enabling the reconstruction of the 3D nitrate field since 2010.

The satellite-derived ocean color data were obtained from the European Space Agency's Global Color Project (Lavender et al., 2009; Stéphane et al., 2010), with a spatial resolution of 25 km and a temporal resolution of monthly (https://hermes.acri.fr). The meteorological driver data were taken from the ERA5 reanalysis dataset (Hersbach et al., 2020) (https://cds.climate.copernicus.eu), with a spatial resolution of 0.25° and the temporal resolution of monthly averaged reanalysis. ERA5 is the fifth generation European Center for Medium Weather Forecasting (ECMWF) atmospheric reanalysis of the global climate. Reanalysis combines model data with observations into a globally complete and consistent dataset. The CMEMS provides ocean dynamics-related data, which has a spatial resolution of 0.25° and a temporal resolution of monthly averages.

2.3 Methods

Figure 2 depicts the process of estimating nitrate and related research in this paper. The SSEVs and spatiotemporal coordinates undergo data preprocessing and resampling (Section 2.3.1) to serve as the feature set for the two-step training of the MLP model. The simulated and BGC-Argo nitrate concentrations provide the constructed MLP model (Section 2.3.2) with labels for two-stage continual learning (Section 2.3.3) training. So far, MLP completes modeling the relationship between the surface environment and internal ocean nitrate. After undergoing four kinds of 3D performance validations, the model reconstructed the 3D nitrate field by inputting iterated spatiotemporal coordinates and corresponding SSEV datasets. The feature contributions and the potential mechanisms for estimation was evaluated based on the training datasets and the model (Section 2.3.5).

2.3.1 Data pre-processing

The candidate input variables for estimating nitrate are depth, latitude, longitude, day of the year, and SSEV data mentioned in Section 2.2.3. The time variables (day of the year) and geographical coordinates (latitude, longitude and depth) are intended to explain the temporal and spatial variations of the studied parameters. The characteristics of biogeochemistry in the ocean properties are described by SSEV such as SST and Chl (D'Ortenzio and Ribera d'Alcalà, 2009). Furthermore, variables such as SSH provide insights into the ocean dynamics, which may contribute to obtaining more accurate vertical stratification.

All these predictor variables are utilized as input features after preprocessing. By standardizing and resampling, they were matched to nitrate concentration measurements, serving as features and labels to train the MLP (Fig. 2b). The potential uncertainty in the input features can be significantly reduced by implicitly incorporating them into the weights of the model when utilizing the same data products (Chen et al., 2019). The gridded SSEV data underwent limited linear interpolation along longitude, latitude, and time, refining localized missing values while filtering out extensive data gaps. Subsequently, the SSEV feature set was linearly interpolated and resampled to align with the spatiotemporal coordinates of nitrate data, ensuring that

Parameter	Description	Unit	Spatial resolution	Temporal Resolution	Data source
Chl	Chlorophyll concentration	mg· m^{-3}	25km	monthly	Globcolour
NFLH	Normalised fluorescence line height	mW·cm^{-2}· microm^{-1}· sr^{-1}			
CF	Cloud fraction	%			
PAR	Photosynthetically available radiation	einstein·m^{-2} ·day^{-1}			
CDM	Coloured dissolved and detrital organic materials absorption coefficient at 443 nm	m^{-1}			
ZHL	Heated layer depth	m			
ZEU	Depth of the bottom of the euphotic layer	m			
ZSD	Secchi disk depth	m			
SST	Sea surface temperature	K	$0.25°$	monthly	ERA5
SP	Surface pressure	Pa			
TP	Total precipitation	m			
Z	Total depth	m			
U10	10 m U wind component	m · s^{-1}			
V10	10 m V wind component	m · s^{-1}			
S10	10 m wind speed	m · s^{-1}			
SSH	Sea surface height	m	$0.25°$	monthly	CMEMS
MLD	Density ocean mixed layer thickness	m			

Table 1. Details of the SSEV dataset.

grid features with missing neighboring coordinates were excluded to prevent low-quality data from adversely affecting model training.

To utilize the annual period, the sampling dates are projected onto the circular coordinates as follows:

$$\mathrm{Jday1} = \cos(2\pi \cdot (\mathrm{dayofyear}/365)), \tag{1}$$

$$\mathrm{Jday2} = \sin(2\pi \cdot (\mathrm{dayofyear}/365)). \tag{2}$$

The other input features are then normalized by applying Z-score transformations as follows:

$$z(x_i) = (x_i - \mu)/\sigma, \tag{3}$$

where μ and i are the mean and standard deviation of each feature of the train set, x_i is the input value of feature i. Z-score transformation is a linear normalization technique commonly used in MLP development to align the inputs and intended outputs within comparable value ranges.

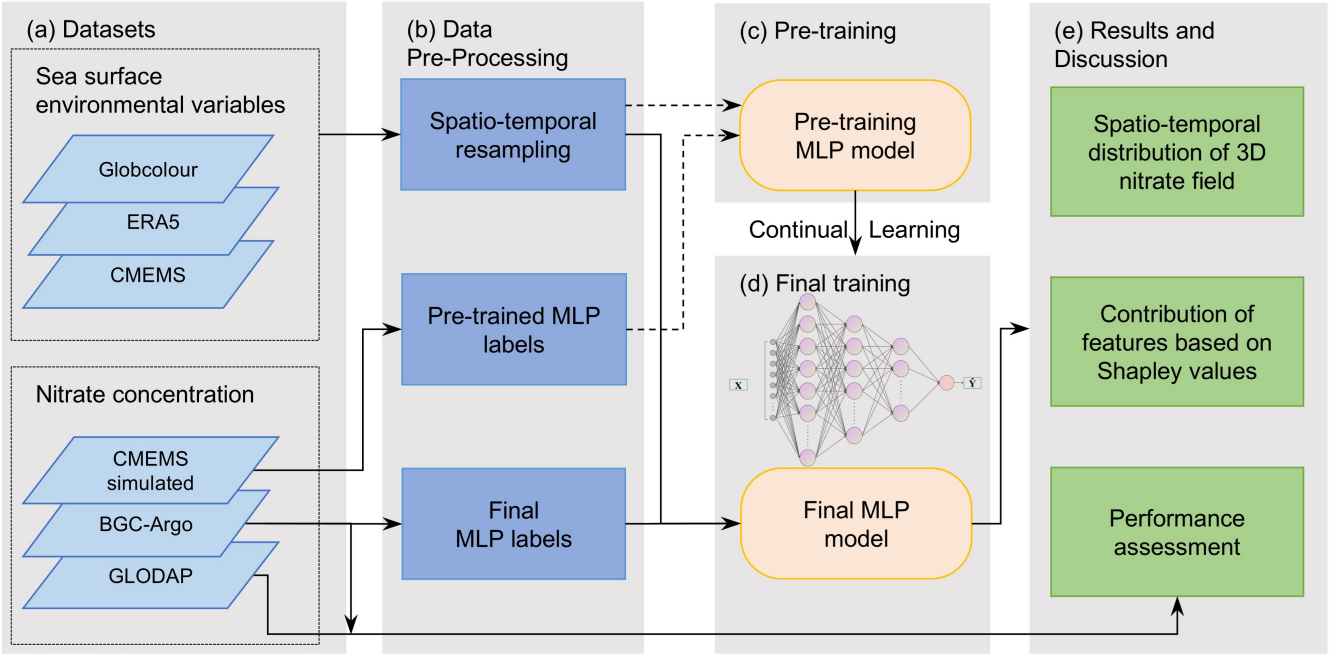

Figure 2. Workflow for nitrate estimation and research on reconstructed results.

2.3.2 Multilayer perceptron

The study develops a Multilayer perceptron (MLP) (Bishop, 1995) model, which is a type of feed-forward neural network that can be used for various types of input or output mappings (Hagan et al., 1997). MLPs can approximate any continuous and derivable function by means of an error backpropagation algorithm (Rumelhart et al., 1986). An MLP consists of interconnected neurons organized into input, hidden, and output layers. Each connection is assigned a weight 'w', and the output is generated by combining inputs and weights using an activation function after adding the neuron's bias 'b_j'. The weights are iteratively updated during the training epochs to minimize the loss function which reduces the quadratic error between MLP outputs and labels. This iterative process continues until a minimum is reached using the approach of error backpropagation.

The structure of the MLP is determined by a series of experiments with multiple hidden layers, and it utilizes the LeakyRelu activation function. The optimal network is determined through multiple trials, where the structure with the least amount of error on the test dataset and the fewest neurons is selected. The final network was configured as (22-128-64-16-1), comprising one input layer with 22 inputs, three hidden layers with 128, 64, and 16 nodes, and one output layer with the nitrate concentration as the output value.

2.3.3 Continual learning

The generalization capability of deep learning models, including MLPs, is highly dependent on the representativeness of the training data. Insufficient or imbalanced training data can exacerbate generalization errors and increase the risk of model overfitting. In the domain of water resource research, challenges associated with the collection of in situ data have highlighted the effectiveness of transfer learning (TL) techniques(Cao et al., 2020; Harkort and Duan, 2023; Miao et al., 2023; Syariz et al., 2020; Zhu et al., 2017). Nevertheless, most TL applications are based on fine-tuning (Ma et al., 2024), which limits their capacity to integrate knowledge from multiple datasets in a more comprehensive manner (Zhou and Zhang, 2023). To overcome this limitation, we developed the continual learning (CL) strategy to improve the training process of BGC-Argo. CL enables the model to assimilate new knowledge continually while retaining previously acquired information, thereby enhancing the robustness and adaptability of the model.

In practice, the simulated nitrate data are initially employed for pre-training, after which the derived network weights are transferred to the subsequent training phase supervised by BGC-Argo observations. Ideally, this sequential process enables the model to capture the general distribution patterns and underlying variation mechanisms present in the simulated nitrate data, and subsequently refine its estimations to achieve higher accuracy using BGC-Argo measurements. However, when the model undergoes incremental training through gradient-based updates, it may experience catastrophic interference or forgetting, leading to the degradation of previously acquired knowledge (Kirkpatrick et al., 2017). To address this issue, Elastic Weight Consolidation (EWC), a regularization-based continual learning algorithm, is applied to constrain weight updates by assigning greater importance to critical network parameters (Kirkpatrick et al., 2017).

Figure 3 (Kirkpatrick et al., 2017) illustrates the effect of training strategies on the two-stage training task and how EWC ensures the retention of knowledge from Task A during the learning of Task B. Sets A and B represent the solution spaces for two training tasks, specifically the simulated nitrate and BGC-Argo training. After completing the Task A, the parameters are denoted as θ_A^*, and the three trajectory lines depict different training processes under varying loss function constraints. Constraining each weight equally (green arrow) imposes excessively rigid restrictions, allowing Task A to be retained only at the cost of failing to learn Task B. Conversely, applying gradient steps based solely on Task B (blue arrow) effectively minimizes the loss for Task B but compromises the knowledge acquired from Task A. Although BGC-Argo measurements are accurate, they are limited in their spatiotemporal coverage for nitrate reconstruction studies, which is insufficient for a comprehensive global characterization of nitrate distributions. Consequently, the center of Set B represents the optimal solution for model weights on the BGC-Argo training set, but which is an overfitted and suboptimal for broader global reconstruction. In contrast, the EWC trajectory (red line) finds an optimal balance for Task B while calculating the importance of weights for Task A, thus ensuring minimal loss in Task A's performance. Robust weights should lie between Sets A and B, balancing the broad and generalizable knowledge from simulated nitrate with the precise measurements from BGC-Argo. This process can be understood as guiding the model to retain the broad knowledge to enhance the generalization ability of Task B, or as calibrating the simulated nitrate with the precision of BGC-Argo. Given that simulated nitrate provides concentration data across the entire

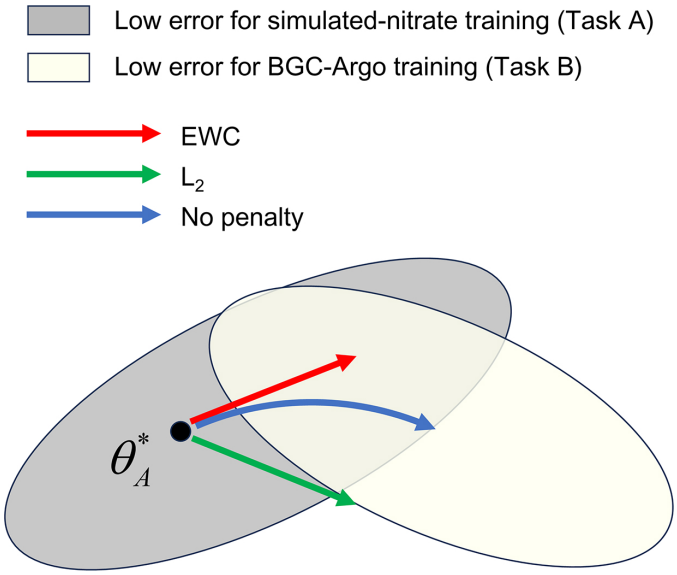

Figure 3. Schematic illustration of how training strategies influence study trajectories in a two-stage task (Kirkpatrick et al., 2017)

.

ocean, especially in regions not yet observed by BGC-Argo, this strategy is crucial for enhancing the generalization capability and robustness of the MLP model.

EWC relies on the Fisher Information Matrix (FIM) to estimate the importance of each model parameter concerning previous tasks (Fisher and Russell, 1997). The FIM quantifies the amount of information that an observable random variable carries about an unknown parameter, reflecting how sensitive the likelihood function is to changes in the parameters.The FIM F is defined as:

$$F = \mathbb{E}_{x,y\sim p_{\text{data}}(x,y)}\left[\nabla_\theta \log p(y|x;\theta) \nabla_\theta \log p(y|x;\theta)^\top\right], \tag{4}$$

where $p(y|x;\theta)$ is the likelihood of the target y of the given data x and model parameters θ, and $\nabla_\theta \log p(y|x;\theta)$ is the gradient of the log-likelihood with respect to the parameters.

In practical applications, computing the full FIM is computationally expensive, particularly for large neural networks. To simplify the computation, it is often assumed that the FIM is diagonal, effectively ignoring dependencies between parameters. In MLPs, the diagonal elements of the FIM can be approximated as follows:

$$F_i \approx \mathbb{E}_{x,y\sim p_{\text{date}}(x,y)}\left[\left(\frac{\partial \log p(y|x,\theta)}{\partial \theta_i}\right)^2\right]. \tag{5}$$

Since the true distribution of data is unavailable, training data is typically used for estimation:

$$F_i \approx \frac{1}{N}\sum_{n=1}^{N}\left(\frac{\partial \log p(y_n|x_n,\theta)}{\partial \theta_i}\right)^2, \tag{6}$$

where, N is the number of training samples, (x_n, y_n) are the data samples, and θ_i is the i-th parameter of the model.

In regression tasks using MLPs, we model the output y as:

$$y = f(x;\theta) + \epsilon, \quad \epsilon \sim \mathcal{N}(0, \sigma^2). \tag{7}$$

Assuming Gaussian noise with constant variance σ^2, the diagonal elements of the FIM can be approximated based on the gradients of the model's output with respect to its parameters. Specifically, we compute F_i as:

$$F_i \approx \frac{1}{N} \sum_{n=1}^{N} \left(\frac{\partial f(x_n;\theta)}{\partial \theta_i} \right)^2, \tag{8}$$

where x_n is the n-th input sample, and $\frac{\partial f(x_n;\theta)}{\partial \theta_i}$ is the partial derivative of the model output with respect to parameter θ_i. This approximation allows efficient computation of F_i during training.

In the Bayesian framework, the goal is to find the parameter θ that maximizes the posterior probability given both the previous task data D_A and the new task data D_B:

$$p(\theta|D_A, D_B) \propto p(D_B|\theta) p(\theta|D_A). \tag{9}$$

Since directly computing $p(\theta|D_A)$ is intractable, we approximate it using a Gaussian distribution centered at the previous optimal parameters θ_A^* with precision given by the FIM (MacKay, 1992):

$$p(\theta|D_A) \approx \mathcal{N}(\theta_A^*, F^{-1}). \tag{10}$$

Taking the negative logarithm of the posterior and ignoring constants independent of θ, we obtain the total loss function:

$$L_{EWC}(\theta) = L_B(\theta) + \frac{\lambda}{2} \sum_i F_i (\theta_i - \theta_{A,i}^*)^2, \tag{11}$$

where $L_B(\theta)$ is the loss for the new task only, i labels each parameter, F_i is the FIM of the previous task, θ_A^* is the optimal parameter value after training on the previous task, and λ is a hyperparameter controlling the trade-off between performance on the new task and retention of the previous task knowledge.

2.3.4 Model validation

Nitrate concentrations derived from the identical vertical observations by BGC-Argo exhibit a strong correlation and a gradual variation with increasing depth. Conventional methods that divide the entire dataset proportionally can result in highly similar data appearing in both the training and test sets, thereby leading to an exaggerated model performance (Salazar et al., 2022). Hence, it is imperative to partition the BGC-Argo dataset based on the observation period, with each period referred to as a profile (Sammartino et al., 2020; Sauzède et al., 2017). This division method ensures the identical distribution and independence of the training and testing sets. Furthermore, the spatial generalization capabilities of the model can be further assessed by partitioning the dataset based on devices.

A 5-fold cross-validation approach is employed to evaluate the model performance using independent test data, which is widely used in machine learning. The BGC-Argo dataset was evenly divided into five subsets, based on profiles or sites. In five distinct cycles, each subset (approximately 20% of the total dataset) served as the test set for one fold, with the remaining four subsets used to train the MLP model. Upon completion of the five folds, all BGC-Argo data were used for one test and four training sessions. This process mitigates the influence of data partitioning bias on performance validation, ensuring maximal data utilization and providing a more robust evaluation of the model's generalization capability. On the test set, the MLP performance was evaluated by comparing the estimated values with in situ nitrate values, using statistical metrics including the determination coefficient (R^2), mean bias error (MBE), mean square error (MSE), root mean square error (RMSE), mean absolute error (MAE), and median absolute error (MedAE).

2.3.5 Evaluating the contribution of inputs

Another major limitation of MLPs and deep learning networks is the lack of interpretability, which makes it challenging to evaluate the estimation processes and mechanisms. However, it is essential to assess the validity of environmental parameters for estimating nitrate concentration, especially since their influence and interactions are not fully elucidated.

The Shapley values (Shapley, 1988) is a method in coalition game theory that effectively describes how benefits are fairly distributed among contributions by the difference between the predicted and average predicted values in each case. The Shapley value of a feature is its weighted and summed contribution to the output over all possible feature combinations:

$$\phi_j\left(val\right) = \sum_{S \subseteq \{1,\ldots,p\} \setminus \{j\}} \frac{|S|!\left(p-|S|-1\right)!}{p!}\left(val\left(S \cup \{j\}\right) - val\left\{S\right\}\right), \tag{12}$$

where ϕ_j is the contribution of the j-th feature to the results. S is a subset of the model's features, and p is the total number of features. $val\left(S\right)$ is the prediction for feature values in S that are marginalized over features not included in S.

Shapley additive explanations (SHAP) (Lundberg and Lee, 2017) is a method for explaining individual estimation results based on Shapley values, which has been successfully applied to evaluate predictors using machine learning algorithms in environmental research (Hu et al., 2023). The purpose of SHAP is to compute the contribution of each feature to the result to explain an instance. The Shapley values are depicted as a linear additive feature attribution approach. SHAP specifies the explanation as:

$$g\left(x'\right) = \phi_0 + \sum_{j=1}^{M} \phi_j, \tag{13}$$

where g is the model to be explained, M is the size of feature space and $\phi_j \in R$ is the feature contribution for feature j, as same as the Shapley values of j.

We can calculate SHAP to quantify the contribution of each feature to the prediction results of a black box model in different samples. The feature tends to increase the output result when SHAP is positive. Conversely, the feature tends to decrease the

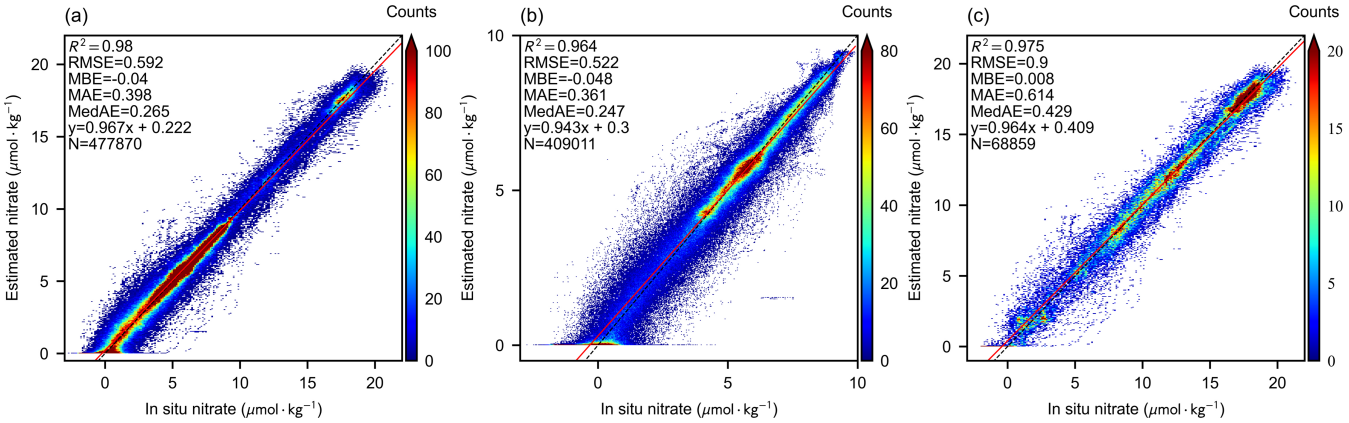

Figure 4. Estimation performance on the test set validated by BGC-Argo measurements (a). The test set results are further divided into the MED (b) and NEA (c) regions. The red line indicates the fitted trend of the data while the black dashed line denotes the 1:1 parity line.

output result when SHAP is negative. Absolute SHAP value (ASV) indicates the degree that the feature affects the output. To observe the overall significance, the mean of ASV for each feature in the data is therefore defined as:

$$I_j = \frac{1}{n}\sum_{i=1}^{n}\left|\phi_j^{(i)}\right|, \tag{14}$$

where i represents data samples, and j represents features.

3 Results and discussion

3.1 Model performance

In the 5-fold profile-based cross-validation, all data is used once in the test set. As illustrated in Fig. 4, the model performance is evaluated by comparing estimated values with BGC-Argo observations. The model demonstrates high accuracy in estimating nitrate concentration, with estimated values generally aligning along the 1:1 line. Importantly, to ensure a comprehensive dataset and enhance the stability of the reconstruction process, we retained all measured labels, including negative values. Furthermore, a Softplus activation function was applied to the model's output layer to guarantee non-negative predictions, albeit at the expense of some degradation in statistical performance metrics. Considering the significant differences between the two regions of the study area, Fig. 4b&c respectively show the test results for the MED and NEA. Compared to the NEA, the MED exhibits a smaller range of nitrate variations and demonstrates stronger estimation performance. The MED records account for 86% of the total dataset, whereas the NEA contributes only 14%. This data imbalance likely contributes to the more consistent performance in the MED compared to the NEA.

While the model has shown satisfactory overall performance, it is critical that the accuracy remains consistently desirable in the vertical dimension. Only then can the model fulfill its intended purpose of estimating and reconstructing the entire 3D

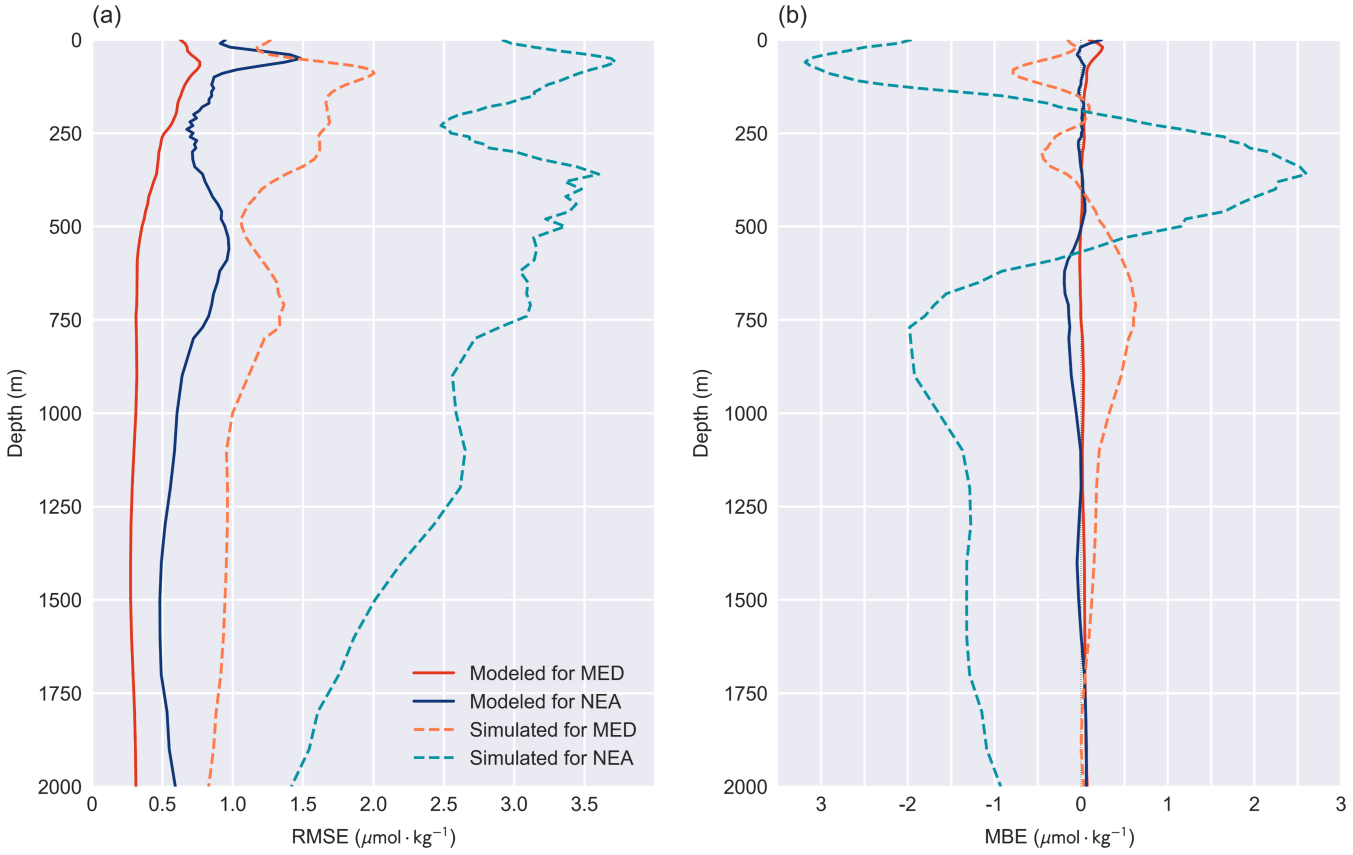

Figure 5. Vertical profiles of RMSE (a) and MBE (b) for modeled and simulated nitrate compared to BGC-Argo measurements.

ocean nitrate field. Figure 5 illustrates the vertical distribution of the primary statistical metrics and their comparison with simulated nitrate. The model maintains robust performance in the vertical dimension, with no significant fluctuations in RMSE and MBE, which is vital for accurately estimating nitrate profiles. The model exhibits slightly superior performance in the MED compared to the NEA at most depths. The RMSE in both the MED and NEA is higher between 0 m and 150 m, with a notable peak at 60 m depth, reaching about 0.8 and 1.4 $\mu mol \cdot kg^{-1}$ respectively. Furthermore, the RMSE of MED remains at a low level and slowly decreases as depth increases. In contrast, the RMSE of the NEA varies drastically, accompanied by a larger overall error, particularly in the 400-700 m depth range. As shown in Fig. 5b, MBE values are negative for most depth ranges in NEA, suggesting a slight overall underestimation of nitrate concentrations, while a slight overestimation occurs in the upper ocean layers of both sub-regions

The model excels in the deep ocean layers beyond 800 m depth, where nitrates are characterized by low variability and minimal feedback from the sea surface environment. Nonetheless, through the use of temporal and spatial coordinates and a dual training process, the model accurately estimates nitrate concentrations. The model's relatively weak performance is observed in the upper 100 m depths, which could be attributed to the sensitivity of the surface layer to external nitrate inputs

(Altieri et al., 2021), thus leading to deviations from the model-fitted relationship between nitrate and SSEV. Furthermore, the ocean at these depths is usually influenced by both the euphotic layer and mixed layers, where complex interactions between ecosystem and ocean dynamics occur, such as water transport, plankton consumption and decomposition. Hence, predicting parameters within this depth has usually presented the biggest challenge in vertical dimension estimation (Sammartino et al., 2020).

In contrast, simulated nitrate exhibits instability in describing the vertical distribution of nitrate concentration. Firstly, simulated nitrate produces significant errors at the ocean surface, possibly due to the limitations of biogeochemical models in simulating complex boundary interactions. However, the estimation error here has been significantly ameliorated by MLP owing to the strong correlation between SSEV and SSN. Secondly, the characterization of nitrate vertical changes by simulated nitrate is not precise enough. The vertical inaccuracy may result in disparities in the characterization of the changes, thus posing a limitation for small-scale biogeochemical research. An evident instance can be observed in the mesopelagic zone (MZ) layer, ranging from 200 to 1000 m in the NEA. Simulated nitrate faced challenges in accurately describing the vertical rate of nitrate variations in this range, resulting in a notable overestimation of nitrate concentrations (Fig. 5b). This is also reflected in the distinct step-like pattern observed at nitrate concentrations of 10-15 $\mu mol \cdot kg^{-1}$ (Fig. 6a) and the overestimation in the vertical pattern (Fig. 8e). Furthermore, MLP and simulated nitrate present similarities in the vertical profiles of RMSE, while MLP consistently outperforms simulated nitrate. This also demonstrates that MLP has improved performance by incorporating prior knowledge from simulated nitrate through CL.

3.2 Spatial generalization ability and enhancement of continual learning

Due to the limited monitoring range of BGC-Argo, the spatial generalization ability of the model is crucial for accurately reconstructing the complete nitrate concentration field. Therefore, this section adopts a more rigorous validation procedure by partitioning the BGC-Argo dataset according to device sites and performing a 5-fold cross-validation as outlined in Section 2.3.4. Under these circumstances, the spatial disparity between the training and testing sets grows significantly, aiding in the assessment of the model's predictive performance across unknown marine regions and amplifying the comparative impact of CL on spatial generalization.

Figure 6e illustrates the accuracy of simulated nitrate concentrations by interpolating gridded simulated nitrate data across longitude, latitude, depth, and time to match the spatiotemporal coordinates of BGC-Argo observations, thereby approximating and validating the simulated values. The results indicate that simulated nitrate tends to form stepwise clusters due to its inertia and lack of variability in representing localized nitrate fluctuations (Fig. 8), leading to similar y-values within subsets that should correspond to x-direction gradients. Nevertheless, the overall agreement between the two datasets remains strong. The simulated nitrate achieves an acceptable accuracy (R^2 = 0.826, RMSE = 1.882 $\mu mol \cdot kg^{-1}$), making it a valuable prior dataset. This compatibility is crucial, and given that simulated nitrate can provide data of comparable accuracy across the entire ocean, its shows great potential as a complement to BGC-Argo data. Simulated nitrate aids in understanding the large-scale distribution of nitrate, offering extensive insights that serves as a beneficial foundation for enhancing fitting relationships during subsequent CL training phases.

Figure 6a illustrates the spatial generalization test performance of the model, demonstrating that CL leads to enhanced test performance, marked by an increase in R^2 of 0.051 and a decrease in RMSE of 0.343 $\mu mol \cdot kg^{-1}$, compared to the non-CL results shown in Fig. 6c. Specifically, the MLP model without CL significantly underestimates high nitrate concentration samples, primarily due to its limited generalization ability in unfamiliar regions of the NEA during site-specific cross-validation. The introduction of CL effectively mitigates this limitation, allowing the model to maintain stable generalized estimates, even for high nitrate concentration samples. Furthermore, the majority of samples exhibit a more consistent fit to the 1:1 line, significantly reducing episodic uncertainty associated with simulated nitrate and the generalization error of the non-CL MLP model. Notably, coupling with CL retains the influence of prior knowledge from simulated nitrate, resulting in localized variability differences. For instance, the densely packed high-concentration samples in warm colors transitioned from symmetric fitting (Fig. 6c) to step-like clustering (Fig. 6a), but achieving a closer fit and overall improved performance. The extent of this transformation is influenced by the EWC parameter λ.

Figure 6b presents the horizontal distribution of RMSE. The predictions exhibit the highest accuracy in the central MED, while larger RMSE values are observed in the NEA and peripheral regions of the MED. The substantial variability in nitrate concentrations in the NEA is largely attributable to the active exchange of eutrophic seawater. Furthermore, the sparse distribution of BGC-Argo measurements in the NEA results in significant deviations from the training data, posing substantial challenges for accurate cross-validation in this region. Overall, high error rates are frequently observed in coastal locations, particularly in the western Strait of Gibraltar and southern parts of the MED. These areas are more susceptible to anthropogenic influences and complex land-sea interactions, which complicate prediction efforts. Additionally, the shallower topography of these regions contributes to increased errors in the vertical water column, particularly in the error-prone ocean surface layer (Fig. 5a).

Notably, regional disparities introduced by CL are evident in Fig. 6d. When the peripheral regions are used as test sets, the discrepancies between training and test data distributions become more pronounced. This sparsity of BGC-Argo data poses a considerable challenge for model estimation in regions lacking sufficient global training on similar datasets, leading to reduced performance metrics. However, CL significantly enhances the model's estimation capabilities in sparsely observed regions, particularly in areas with high RMSE near the boundaries of BGC-Argo coverage. This suggests that CL helps reduce model instability when generalizing to unfamiliar regions by incorporating prior knowledge from simulated nitrate. For instance, in the western Strait of Gibraltar, complex environmental interactions and similarities in spatial coordinates with the MED present significant estimation challenges. Nevertheless, the model demonstrates substantial improvements in both accuracy and generalization stability compared to the MLP without CL. Moreover, the model achieves more accurate estimates by fitting BGC-Argo data, showing a comprehensive improvement over simulated nitrate (Fig. 6f), which is critical for reconstructing the three-dimensional nitrate field. Interestingly, in data-dense regions such as parts of the Mediterranean, the incorporation of CL results in a slight increase in RMSE. This phenomenon occurs because, in well-sampled regions, prior knowledge may interfere with the MLP's fitting process. However, the influence of this prior knowledge can be optimized by regionally adjusting the EWC parameter λ. Currently, this parameter has been selected to achieve an overall optimal performance.

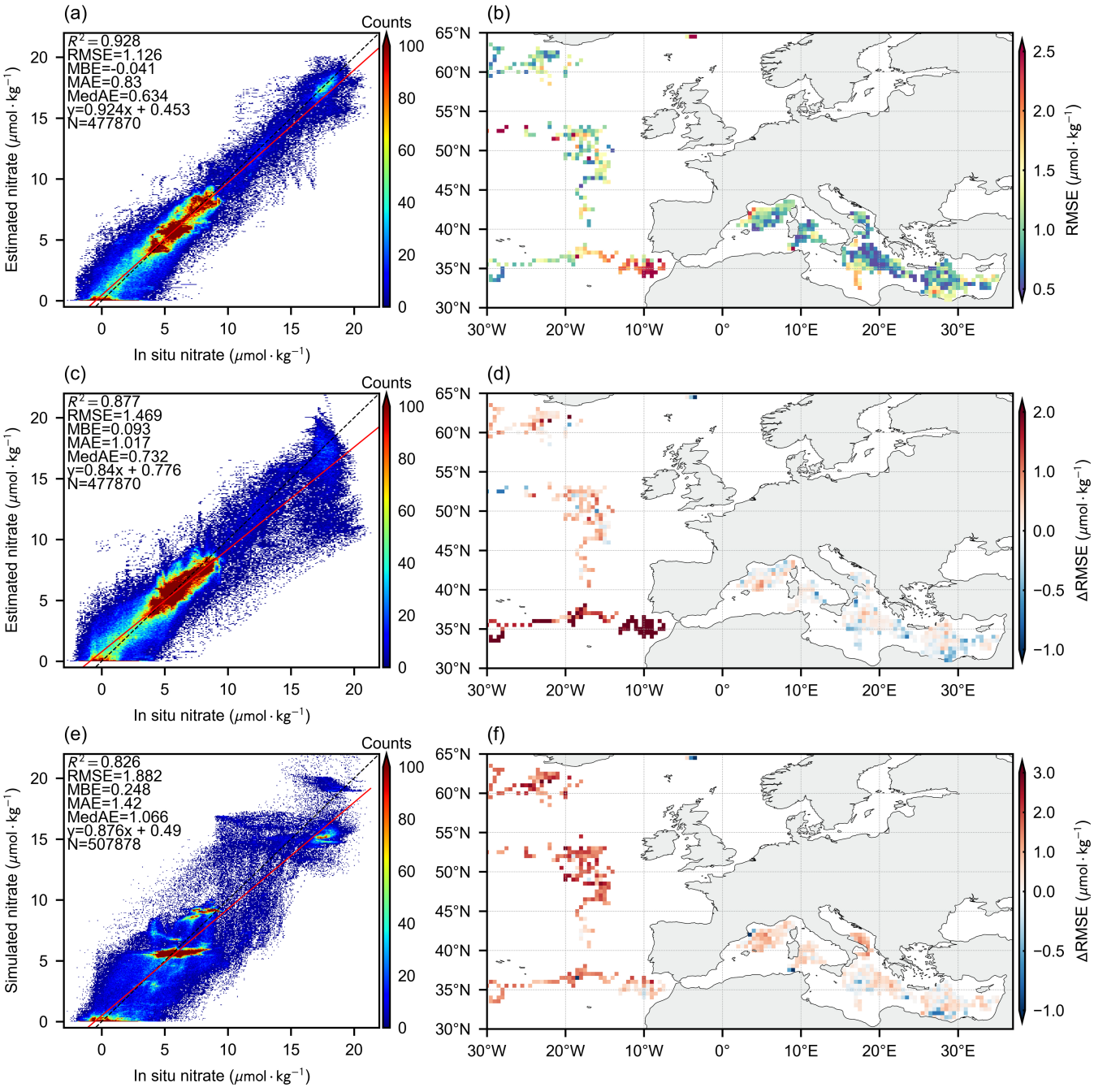

Figure 6. Illustration of Model performance and spatial generalization in site-based cross-validation (a) and spatial error distributions (b), compared with the case without CL (c-d) and the case of simulated nitrate itself (e-f). Subplots show: (a) test performance with CL; (b) spatial distribution of model accuracy; (c) test performance without CL; (d) distribution of RMSE increase (non-CL relative to CL); (e) validation performance of simulated nitrate concentrations; and (f) spatial distribution of RMSE increase (simulated nitrate relative to model with CL).

In conclusion, it is reasonable to infer that CL enhances the overall model performance and generalization capability in regions not covered by BGC-Argo by incorporating relevant knowledge and patterns from simulated nitrate. This process is influenced by data distribution and weighting parameters.

3.3 Independent validation with GLODAPv2

To further ensure a more stable assessment of the model's generalization ability in data-sparse regions while avoiding potential autocorrelation within the BGC-Argo dataset, the GLODAPv2 dataset was employed for independent validation, which was not involved in training. Fifteen cruises measuring nitrate concentrations at depths ranging from 0 to 2000 m in the study area were selected, and their measurements were compared against model estimates and simulated nitrate. Figure 7c illustrates that a significant portion of the GLODAPv2 data is located in the NEA, thereby allowing for an effective assessment of the model's performance in under-sampled regions. The results indicate a strong correlation with the GLODAPv2 nitrate concentrations, as evidenced by an R^2 value of 0.94 (Fig. 7a).

Figure 7c also depicts the regional distribution of errors, revealing that model performance varies significantly across different regions. The lowest errors are observed in the western MED and the southern NEA, whereas larger errors are concentrated in areas with sparse BGC-Argo observations. This distribution pattern and its underlying causes align with the spatial performance in site-based cross-validation, as shown in Fig. 5b. Factors such as enhanced water exchange dynamics (Berglund et al., 2023), intricate land-sea interactions, and shallow topography contribute additional complexities. Moreover, several expeditions north of 50°N occurred in 2010 - 2012 and 2015, while most BGC-Argo observations in the same region were conducted post-2020. The pronounced variability of nitrate concentrations in the NEA, coupled with limited observations and temporal discrepancies, diminishes the data representativeness, leading to increased RMSE. Overall, the error margins are deemed acceptable and still outperform the validation accuracy of simulated nitrate (Fig. 7b).

3.4 Validation of three-dimensional nitrate pattern

To thoroughly examine and contrast the seasonal vertical patterns of BGC-Argo, modeled, and simulated nitrate, two representative regions depicted in Fig. 1 were selected to facilitate a comprehensive evaluation of the model's efficacy. The Box NEA, situated at 14-19° W and 46-53° N, and the Box MED, located at 26-30° E and 32-36° N, were chosen due to their frequent BGC-Argo sampling, which ensures high consistency between measured data and observed vertical patterns. The vertical distribution of nitrate is depicted in Fig. 8 for these two regions, where the MLP model, simulated nitrate, and BGC-Argo observations are juxtaposed for comparison.

The reconstructed vertical nitrate profiles derived from the MLP model demonstrate greater consistency and robustness compared to BGC-Argo data, whereas the profiles from simulated nitrate still exhibit significant discrepancies in capturing seasonal variations. The MLP model has shown a remarkable ability to capture mid-scale features, such as the seasonal increase during winter and decrease during summer, aligning well with BGC-Argo data and effectively depicting seasonal variations in the upper ocean. Furthermore, the MLP model is consistent with BGC-Argo in representing depth-dependent variability within the Mesopelagic Zone (MZ), while bridging gaps left by the intermittent nature of BGC-Argo measurements. In contrast,

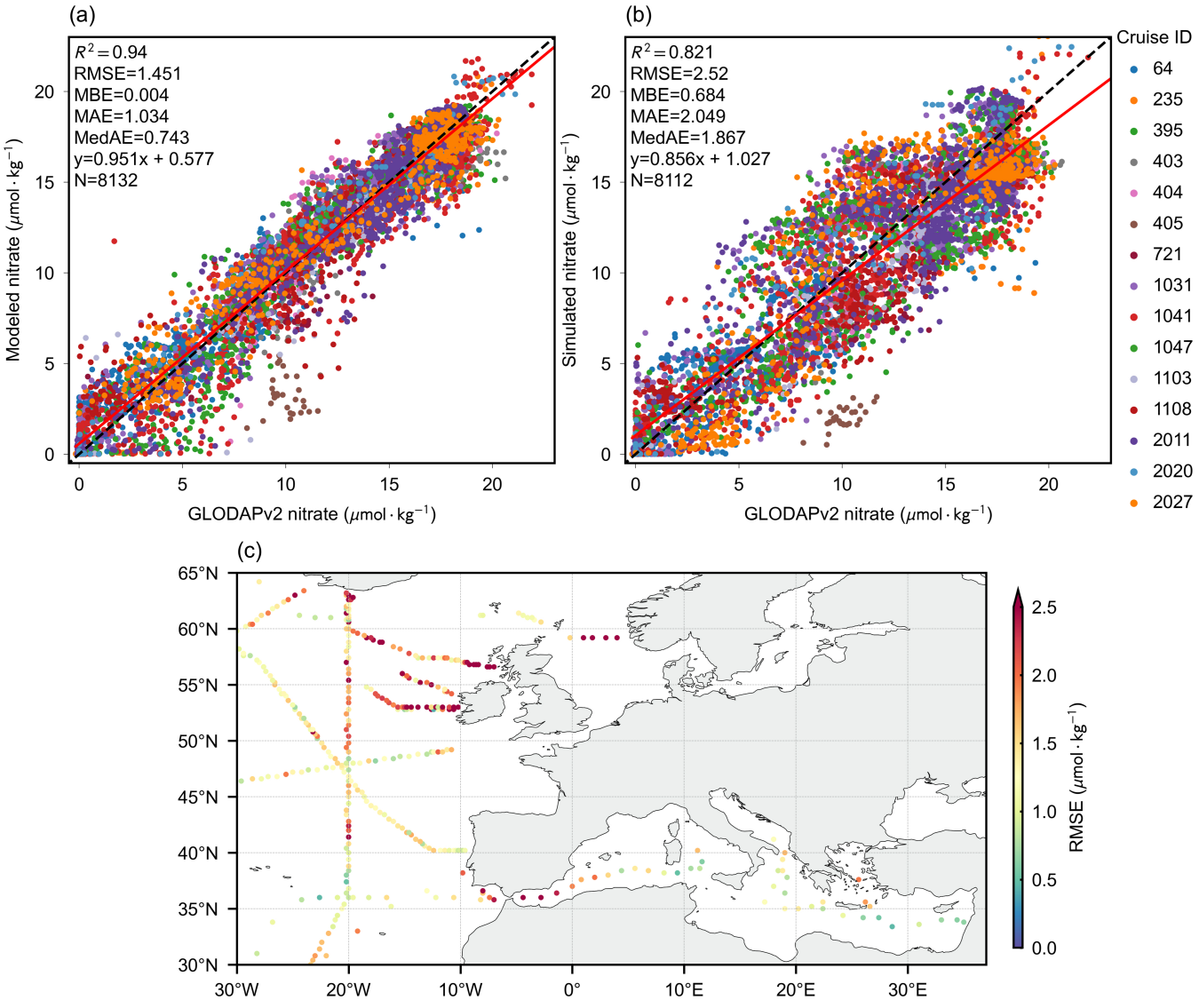

Figure 7. Accuracy comparison between MLP-estimated nitrate (a) and simulated nitrate (b), using GLODAPv2 measurements for validation, with colors denoting individual cruises. Subplots show: (a) validation of MLP-estimated nitrate; (b) validation of simulated nitrate; and (c) spatial RMSE distribution of MLP-estimated nitrate, where the errors are derived from the average vertical measurement error at each cruise sampling location.

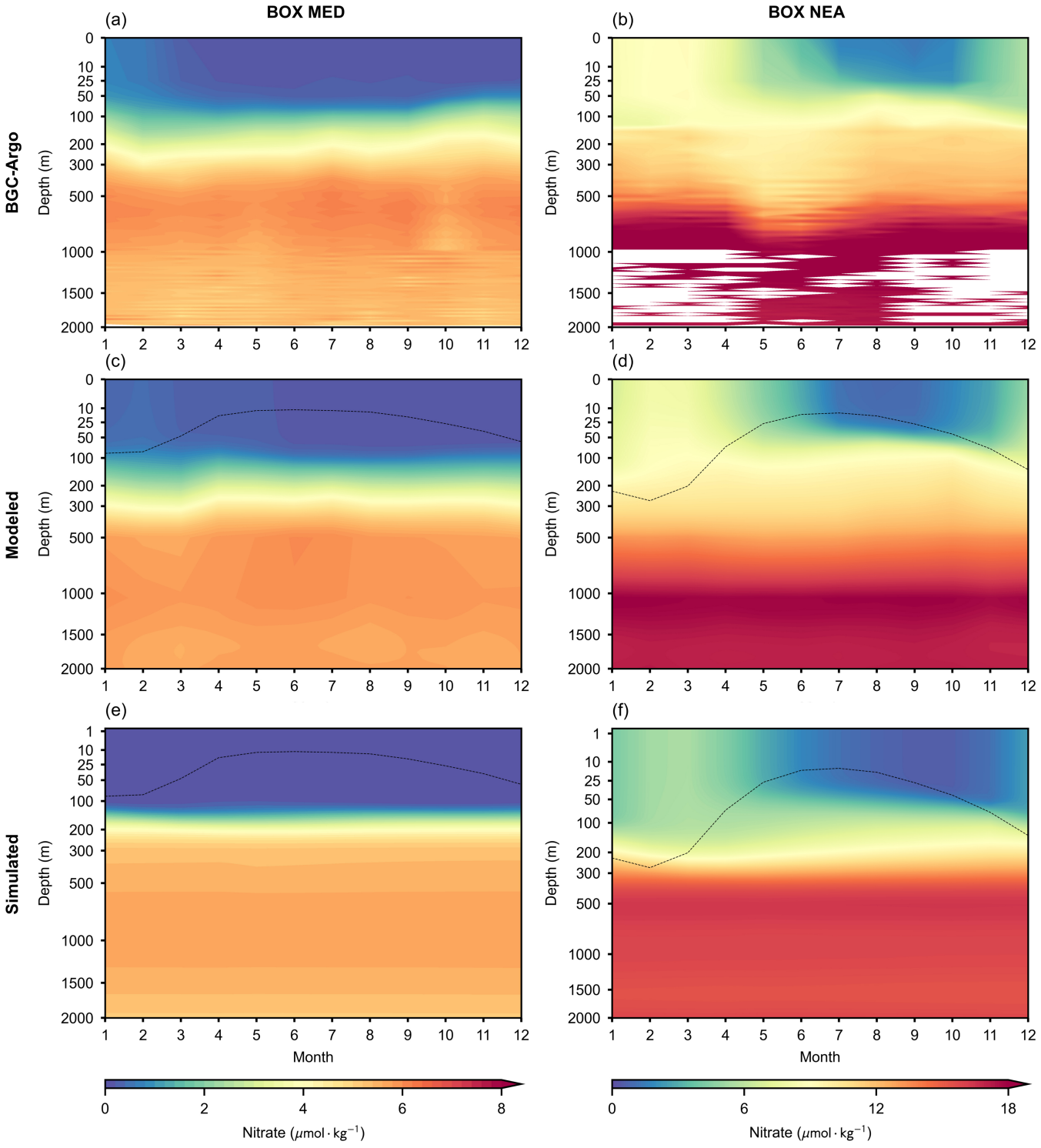

Figure 8. Comparison of monthly vertical patterns of nitrate in the designated region among BGC-Argo, the MLP model, and simulated climatology. (a), (c), and (e) correspond to the box MED, while (b), (d), and (f) correspond to the box NEA. The black dashed lines represent the average MLD from the CMEMS dataset.

simulated nitrate tends to underestimate concentrations in the upper ocean (Fig. 5b) and shows relatively sluggish seasonal variations, including the absence of a pronounced increase during winter in Box NEA and insufficient representation of seasonal changes in the upper layers of Box MED.

As previously discussed, the model's estimation results demonstrate satisfactory accuracy and strong performance on the test dataset. Additionally, the model's predictions have been analyzed comprehensively across vertical, horizontal, and temporal dimensions, all indicating high performance. To ensure robust generalization across diverse oceanic environments, the joint model was employed to estimate nitrate concentrations in both the MED and NEA, despite facing specific challenges. Given the complexity of the marine environment and the fact that the NEA represents only 14% of the dataset, a higher error rate in this region is acceptable. Despite increased errors in some challenging cases, the model generally proves to be a reliable approach for reconstructing the 3D nitrate concentration field.

3.5 Spatial and temporal distribution of the reconstructed nitrate field

The reconstruction of the 3D nitrate field from 2010 to 2023 was conducted using the MLP model combined with the SSEV for the corresponding period. The reconstructed field features a monthly temporal resolution, a horizontal spatial resolution of 0.25 degrees, and 63 depth levels, with vertical intervals ranging from 5 to 50 m. Figure 9 illustrates the spatial distributions of the reconstructed nitrate at various depths across the pan-European region, with representative profiles selected at depths of 0, 50, 100, 150, and 500 m.

The reconstructed nitrate field reveals substantial spatial variability, with a clear increasing trend in nitrate concentrations with depth. The MED identified as an oligotrophic region, generally exhibits nitrate concentrations below 5 $\mu mol \cdot kg^{-1}$ at depths between 0 and 150 m. Unlike the NEA, the MED nitrate concentrations are less influenced by seasonal dynamics, primarily due to the region's enclosed nature and restricted seawater exchange. The oligotrophic characteristics of the MED intensify from west to east, with more pronounced differences evident in the deeper ocean layers (Pujo-Pay et al., 2011; Ribera d'Alcalà et al., 2003). In contrast, the NEA is characterized by higher nitrate concentrations and pronounced seasonal variability, which is largely driven by the influx of nutrient-rich water masses from the open ocean (Berglund et al., 2023). The highest nitrate concentrations are found in the northern NEA seawaters, a typical eutrophic region. The spatial pattern of the reconstructed results aligns well with that of the simulated nitrate dataset overall (Fig. S1), including extensive regions not covered by BGC-Argo, such as the coastal waters of the UK and Norway. Meanwhile, discrepancies are observed in certain small-scale 3D structures between the reconstruction and the simulated nitrate field. These differences have the potential to provide valuable data foundations and insights for further ecological research.

Figure 10 presents the temporal-depth profiles of nitrate concentration as a function of the month in both the MED and NEA, allowing for a more detailed examination of their temporal patterns. The seasonal variability of nitrate in the MED is relatively subtle. During winter, upwelling of nutrient-rich cold water elevates nitrate concentrations in the upper ocean, with a marked increase observed from October to February of the following year. After reaching this peak, nitrate levels decline due to phytoplankton uptake during spring, followed by a secondary rise in autumn as phytoplankton biomass decays (Severin et al., 2017). Conversely, the NEA exhibits a pronounced temporal pattern in nitrate concentrations, primarily governed by ocean

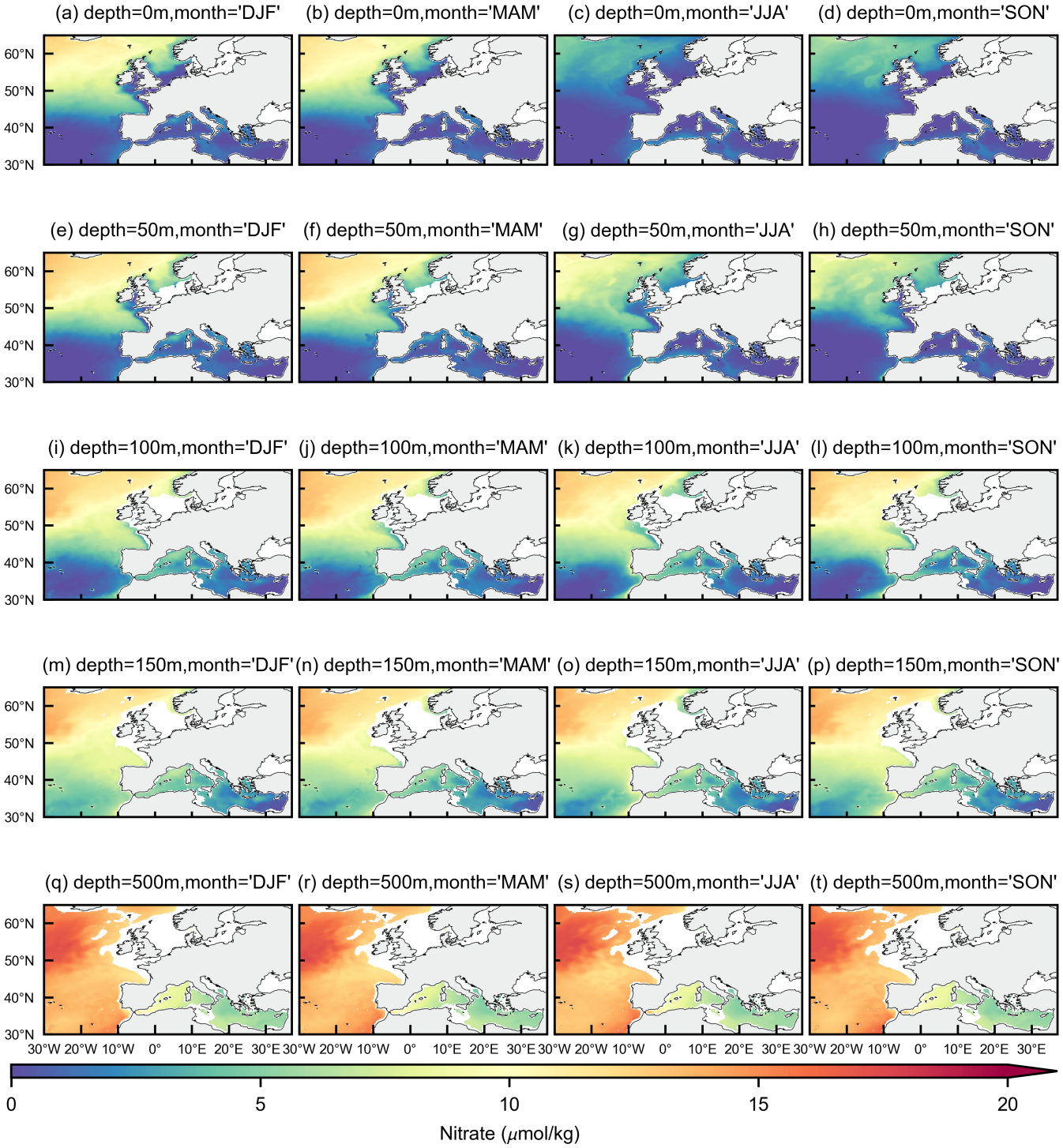

Figure 9. Spatial distribution of reconstructed nitrate field, with columns representing four seasons and rows representing five depth slices.

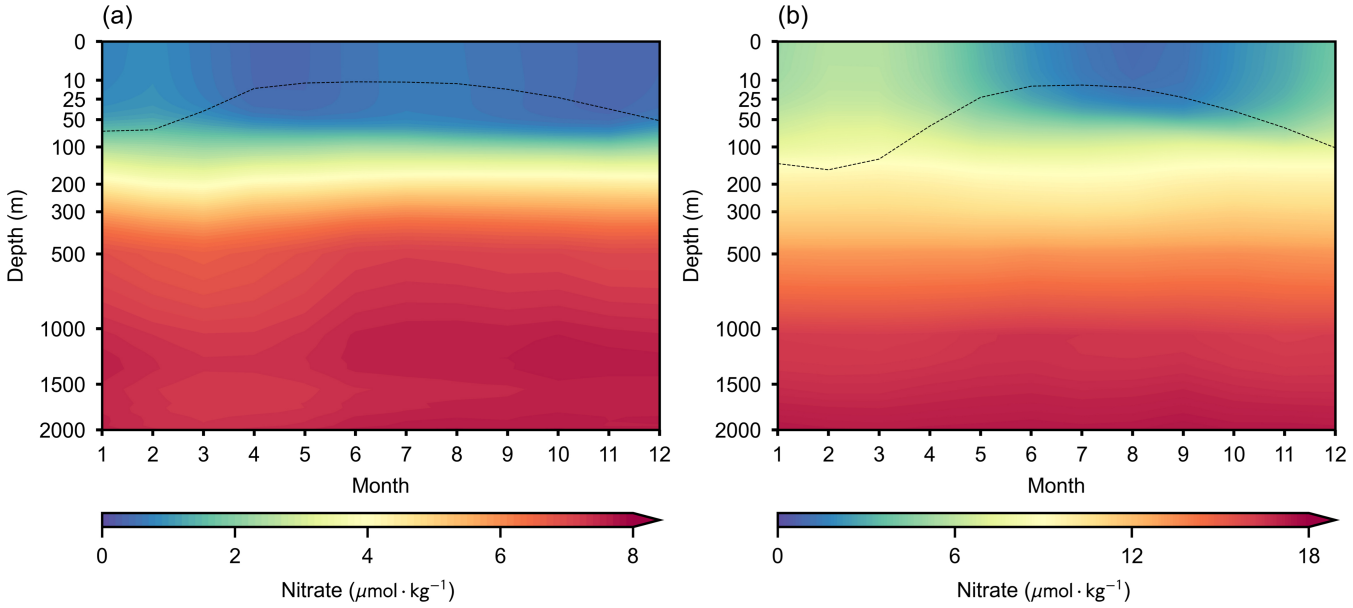

Figure 10. Monthly distribution profiles of nitrate concentrations in the MED (a) and NEA (b). The black dashed lines represent the average MLD from the CMEMS dataset.

dynamics. In the mixed layer, from the surface to approximately 100 m depth, nitrate levels increase from October to March and subsequently decrease from April to August. The temporal pattern in the NEA resembles the winter increase observed in the MED but lacks a distinct secondary peak, instead showing a more sustained high-nutrient period.

Figure 11 illustrates the interannual anomalies of nitrate concentrations across the study area, derived by subtracting the annual mean nitrate value for each year from the monthly nitrate concentrations. In most instances, nitrate anomalies exhibit consistency throughout the vertical profile, with this uniformity being more pronounced in the MED. Additionally, episodic discontinuities are often detected at depths around 100 m and approximately 500 m, corresponding to the mixing layer and certain pycnoclines. In the NEA, where seawater exchange is more dynamic, discontinuities in nitrate concentration are more prevalent. Compared with existing data sources, although BGC-Argo and simulated nitrate represent some of the most advanced nitrate data available from current observational and numerical models, they still face significant challenges in depicting interannual trends (Fig. S2). Due to the varying geographical locations of BGC-Argo observations over time, regional differences in nutrient levels introduce considerable interference and fluctuations in the calculation of interannual trends. Consequently, the trends presented by BGC-Argo appear more radical and may even be reversed if the sampling locations encompass both high- and low-nutrient regions. As for CMEMS nitrate, its response to mesoscale nitrate variations is relatively sluggish, leading to an overly homogeneous trend that is likely more conservative than the actual scenario. Nevertheless, its overall trend can serve as a reference for multi-year scale variations, such as the increasing nitrate levels in the MED and the intensified downward deposition of upper ocean nitrate in the NEA (Fig. S2).

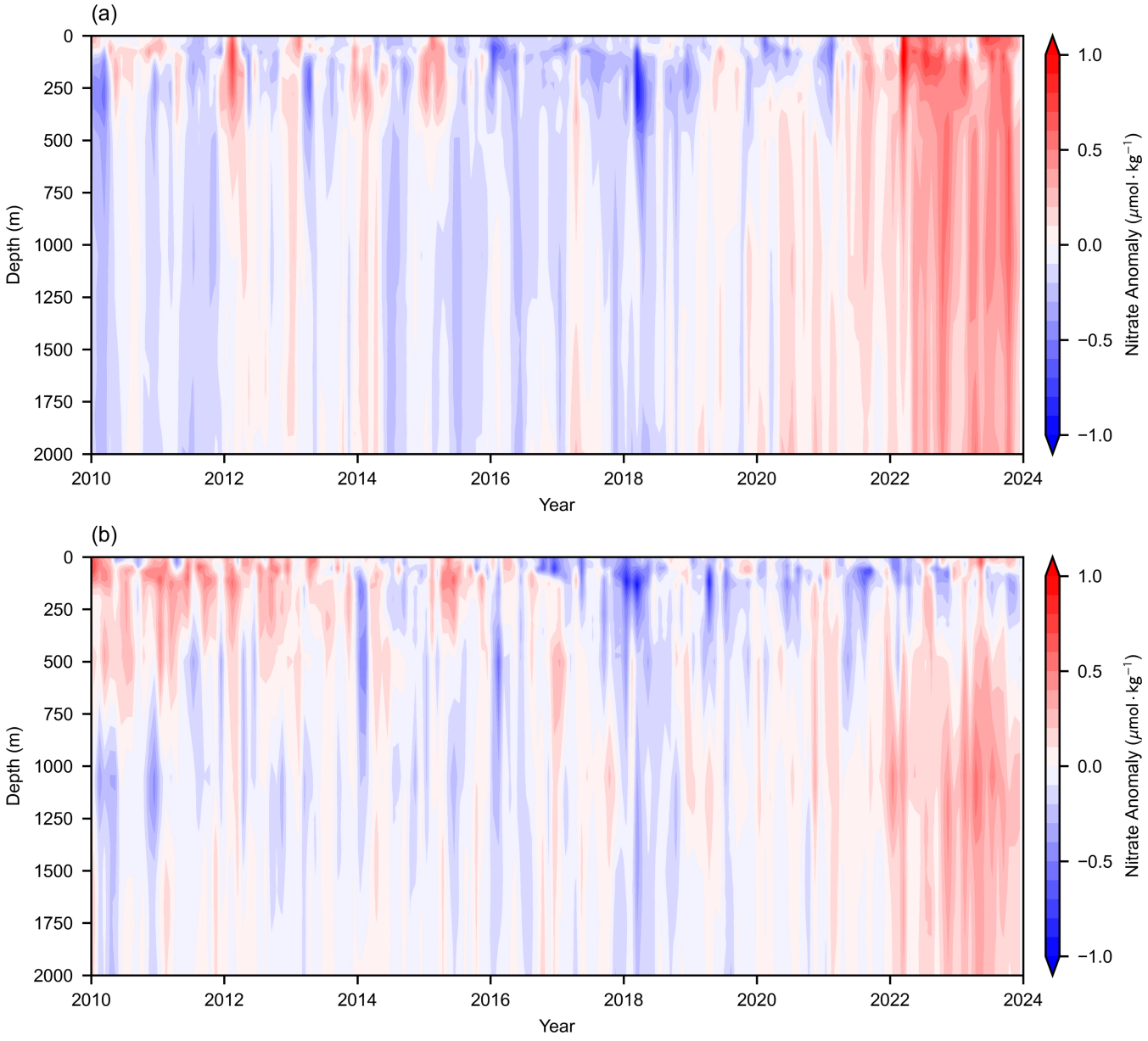

Figure 11. Interannual anomaly profiles of reconstructed nitrate concentrations in the MED (a) and NEA (b).

This study identifies three significant temporal trends. Firstly, there is a discernible overall increase in nitrate concentrations, characterized by more frequent positive anomalies, particularly since 2021. This trend indicates an increasing fluctuation in nitrate levels and an escalation in eutrophication within the study area. The reconstruction outcomes align closely with trends observed in various case studies, and extend these observations by providing results on a broader scale with more detailed quantification.

The MED exhibits a notably regular upward trend. BGC-Argo sequence analyses from the Sicily Channel revealed a slightly negative nitrate trend from 2011 to 2016, shifting to a positive trajectory thereafter until 2020 (Fourrier et al., 2022) . In simulations employing physical-biogeochemical models under Representative Concentration Pathways (RCPs) 4.5 and 8.5 scenarios for the northwestern MED, nutrients displayed a general ascending pattern, notably more pronounced in deeper ocean layers than in surface waters (Reale et al., 2022). Remarkably, an anomalous nutrient surge after 2022 could potentially be linked to the severe winter storm Carmel in 2021. A detailed time-series analysis over four years at the Levantine basin site demonstrated substantial replenishment of marine nitrates during the 2021 winter storm, reversing a declining trend initiated in 2018 (Ben-Ezra et al., 2024). By contrast, interannual anomalies in the NEA are significantly more volatile. Although certain hypotheses suggest that intensified ocean stratification due to climate warming could limit nutrient availability in the upper ocean layers, recent findings indicate this limitation primarily affects phosphates, whereas nitrates continue to exhibit frequent and pronounced local fluctuations. The reconstruction results provide meticulous trend characterizations, consistent with documented positive anomalies observed in NEA upper ocean layers between 2010 and 2014 (Macovei et al., 2019), as well as the identified growth patterns within the Iberian upwelling system (Padin et al., 2020).

Secondly, while vertical consistency of nitrate anomalies is stronger in the MED compared to the NEA, a decline in upper ocean nitrate concentrations is evident in the NEA. Ocean warming has hindered the upward transport of nutrient-rich cold water, modifying the vertical nitrate distribution in the NEA. Moreover, no consistent overall trend of anomalies is apparent in surface nitrate concentrations in the NEA, which may be driven by complex ocean-atmosphere interactions and anthropogenic influences. Thirdly, the transition period of nitrate anomalies appears to be lengthening. The duration of individual positive or negative anomalies has extended from a few months at the beginning of the study period to several months or even over a year. This lengthening may indicate irreversible shifts in the marine environment or a decline in the ocean's self-regulatory capacity.

Furthermore, interannual anomaly trends must be interpreted cautiously due to their dependence on SSEVs and specific weights of the model, and their reliability requires further research. For instance, the reconstructed results may overestimate anomalies in the Bathypelagic Zone (>1000 m). At these depths, nitrate concentrations are relatively stable (Fig. 10) and are not effectively represented by SSEVs. Nonetheless, the model's estimates are inevitably influenced by the SSEV signal. The accuracy of these anomalies is significantly influenced by both the generalization capacity of the model and the stability of the input features. Despite the model's proven reliability, particularly with the MEB performance most relevant to anomaly calculations consistently maintaining an excellent level of $\pm 0.04\ \mu mol \cdot kg^{-1}$ across multiple validations, small-scale findings still require further corroboration through targeted case studies. Overall, compared to the limitations posed by the discontinuous, discrete observations from BGC-Argo and the inadequacies of simulated nitrate in capturing fine-scale variability, the reconstructed dataset offers an encouraging and comprehensive perspective for trend analysis.

3.6 Contribution of features to the model output

The current model is established based on all available features in the dataset, but given the redundancy among these features, the model may require fewer of the most efficient features. There are two benefits to entering all mentioned features. The ability of MLP to automatically extract features ensures that the model will be enhanced and minimally affected by feature redundancy.

Particularly, the utilization of large-scale simulated nitrate data has significantly contributed to the model's capability to capture non-linear relationships among multiple features, thus enabling it to effectively monitor nitrate concentration across a wide range of SSEV scenarios. On the other hand, analyzing the importance of each feature based on the model with all the input features is crucial for further studies of nitrate estimation.

Figure 12 depicts the Pearson correlation coefficients among the features. Nitrate has been found to be positively correlated with depth and Chl, and negatively correlated with SST (Yu et al., 2022). Furthermore, nitrate is also positively correlated with features such as CDM, NFLH and Si10, and negatively correlated with features including ZEU, ZHL, and ZSD. The spatial distribution is characterized by a positive correlation with latitude and a negative correlation with longitude, since nitrate concentrations in the NEA are generally higher than in the MED. Diverse relationships among the input features suggest the potential for feature redundancy, exemplified by the marked positive correlation between SST and ZHL, and the negative correlation between ZSD and Chl. The correlation coefficient can only capture linear relationships between variables, while MLP is a model to fit nonlinear relationships. Therefore, the contribution of features to results cannot be determined solely based on correlation coefficients. The contributions of features based on SHAP values are discussed next.

Given the high computational cost of SHAP (Chau et al., 2022) and the sufficient representativeness of a smaller sample (Pauthenet et al., 2022), we randomly selected 200,000 samples to estimate feature contributions. Figure 13 illustrates the probability distribution of SHAP values for each feature, with features ranked according to their average ASV. Given the different mechanisms by which features affect the ocean at various depths, the ocean is divided into two layers in the contribution discussion. Bounded by the 200 m depth, the upper layer is the Epipelagic Zone (EZ), and the deeper layer of 200-2000 m is the Mesopelagic Zone and part of the Bathypelagic Zone.

The input spatial features include depth, longitude, and latitude. Among them, depth is consistently identified as the strongest feature extracted by the model, which corresponds to the pattern of variations in the vertical distribution of nitrate , as depth uniquely facilitates the mapping of nitrate profiles (Fig. S3). Particularly in the EZ, the contribution of depth features is extremely significant with $I^{\mathrm{EZ}}_{\mathrm{Depth}} = 2.36$, surpassing that of other features and also much larger than the contribution of depth in the 200-2000 m depths. This is attributed to the fact that the increase in nitrate concentration with depth is most pronounced in the EZ. The nitrate concentration at 200 m depth may be several times higher than that at the sea surface. Although such a trend is also observed in 200-2000 m depths, the magnitude of this change is relatively small. Hence, depth always remains the most crucial feature, especially in the EZ.

Furthermore, longitude is the second essential feature in the model. Nitrate concentration in the MED and NEA differs greatly, resulting in longitude more vital than latitude. In the 200-2000 m depths, the contribution proportion of spatiotemporal coordinates increase, while the contributions of other SSEV features decrease. On the one hand, nitrate concentration in the surface ocean is more susceptible to SSEVs. On the other hand, nitrate in the deep ocean exhibits low seasonal variability but stable regional characteristics, and its concentration is primarily related to its location. The estimation process in the deeper ocean mainly relies on spatiotemporal coordinates, supplemented by subtle adjustments in environmental variables.

The feature ranking in Fig. 13 closely aligns with that in Table S1, though there are some minor differences. Both discuss the importance of features, but the SHAP values in Figure. 13 focus on the contributions of features, while the RMSE changes

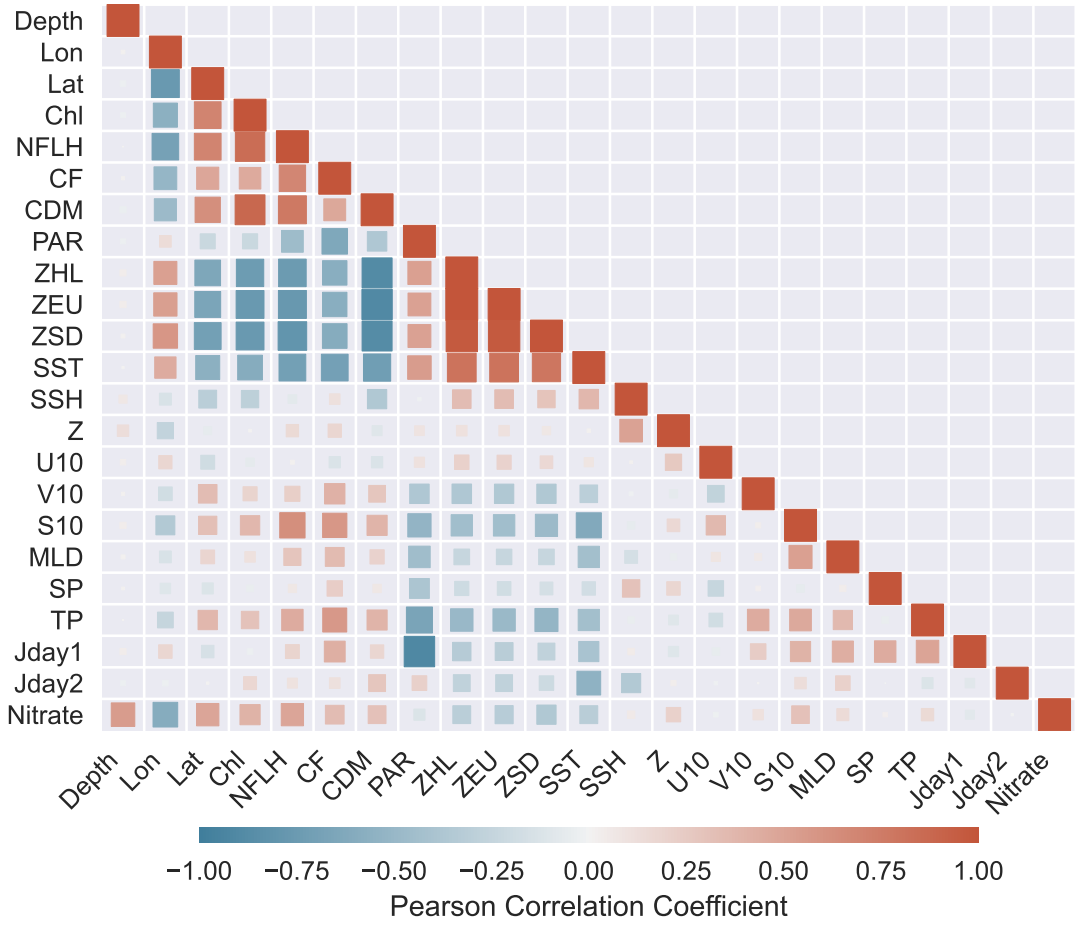

Figure 12. Heatmap for the matrix of Pearson correlation coefficients between nitrate and input variables. The size of the cell represents the absolute value of the correlation coefficient.

in Table S1 emphasize the irreplaceability of features. For example, Z (Total terrain depth), which provides a unique perspective, has a small contribution but significantly impacts the model when excluded. Furthermore, when excluding features, we combined Jday1 (the cosine function of the Julian day) and Jday2 (the sine function of the Julian day), which have a high contribution but a minimal impact on model performance when excluded. This is because Jday is a heuristic feature that, while useful for providing temporal information, can be inferred through the periodic variation of other variables. Figure 12 shows the correlation heatmap between nitrate and all input variables. The current feature combination is sufficient and potentially redundant; some highly correlated features can substitute one another to some extent, which is why the RMSE increase after excluding high-contribution features like PAR is relatively small. However, the comparison experiments in Table 1 confirm that the model can accommodate these correlated features and enhance its performance.

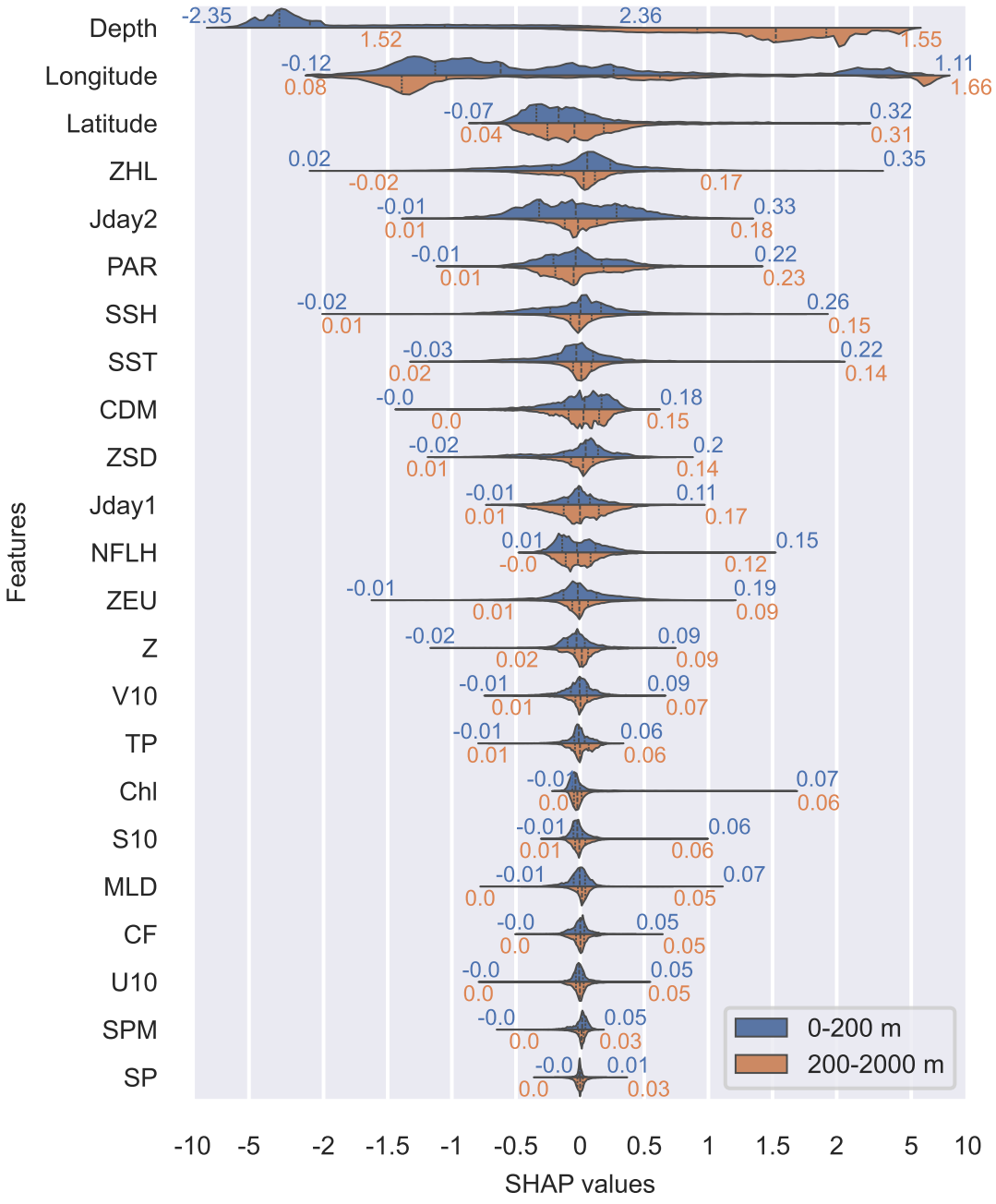

Figure 13. Probability distribution of SHAP values representing the impact of each feature on the model output. The y-axis shows the input features, sorted by the total magnitude of I_j, while shaded area in the x-axis direction represents the distribution of SHAP values, scaled due to the large range. The numbers labeled on the left show the mean of the raw SHAP values, while those on the right show the mean of the ASV. The black vertical dashed lines represent the median and quartiles of the SHAP values.

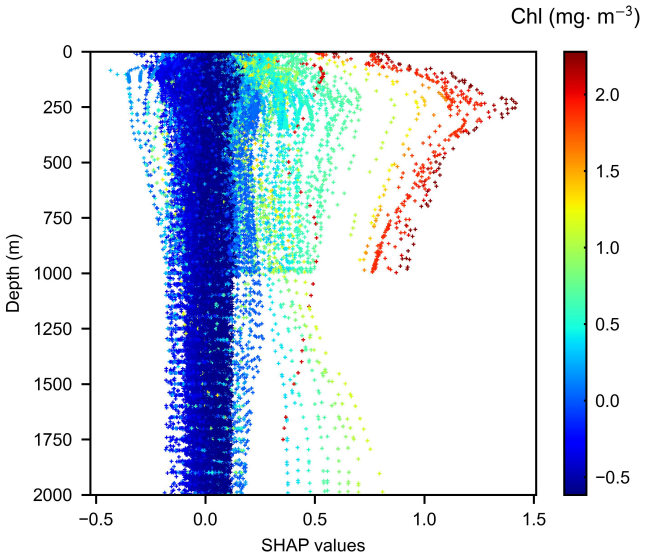

Figure 14. Scatter plot of Chl contribution values across data samples. The x-axis represents SHAP contribution values, while the y-axis represents depth. The color of scatter points indicates the Chl feature values in each sample.

The residual features comprise environmental parameters, which encompass diverse facets of climate, biology, and ocean dynamics. Among these parameters, SSH exhibited a notably higher I_j, value, and demonstrated the most significant impact on model performance when excluded (Table S1). SSH reflects various dynamic effects of ocean circulation, mixing layers and eddies, which together influence the horizontal and vertical transport of nitrates (Ascani et al., 2013; Fripiat et al., 2021; Sarangi and Devi, 2017; Wang et al., 2021). SSH reflects the influence of ocean dynamic variability on nitrate concentrations, typically exhibiting opposing impacts between the EZ and deeper ocean.

Another set of critical features comprises SST-related variables. SST exhibits strong correlations with ZHL, PAR, and ZSD (Fig. 12), each concurrently presenting high I_j values, underscoring the dominant role SST-related features play in nitrate estimation processes. Highly correlated features may dilute their individual contributions to the results, thus SST may have a more significant role than depicted in the Fig. 13.

Previous studies have established SST as a principal environmental factor for nitrate retrieval, highlighting upwelling and winter convective mixing constitute two crucial physical processes that drive the transportation of cold, nitrate-rich waters into the euphotic layer, thereby boosting SSN and simultaneously reducing SST (Kudela and Dugdale, 2000; Pan et al., 2018). Since SST and SSH provides information on vertical mixing, its contribution in the deep ocean remains significant compared to other SSEVs. Among them, ZEU and PAR are indicative of the optical environment as well as NLFH and CF, probably related to the oxidation of nitrogen by light inhibition and the activity of phytoplankton (Hutchins and Capone, 2022; Zakem et al., 2018). Furthermore, ocean dynamics parameters (e.g., MLD and S10) also contribute to nitrate estimation by influencing nutrients in multiple ways (Tuerena et al., 2019; Liu et al., 2019).

Notably, Chl has previously been employed as another pivotal variable for SSN retrieval (Goes et al., 1999; Pan et al., 2018; Sarangi and Devi, 2017). However, in both the EZ and deeper layers, its average contribution remains relatively low, exhibiting instead a distribution characterized by a long tail of positive values. This phenomenon aligns closely with feature assessments in nitrate reconstruction in the Indian Ocean Yang et al. (2024) and dissolved organic nitrogen studies in the Atlantic (Altieri et al., 2016). The predominant limiting factor is the confined spatiotemporal scope; although Chl is intrinsically linked with nitrate, its positive contributions are restricted primarily to biologically productive upper layers vertically, and horizontally confined nutrient-rich regions, where only comprises a small portion of the oceanic 3D field. Consequently, regions minimally influenced by Chl dilute the average contribution of phytoplankton across broader oceanic estimations. Figure 14 illustrates the distribution of Chl contributions across specific samples. In the majority of cases, low chlorophyll concentrations yield negligible effects, while slight increases in Chl typically exert a negative influence, as phytoplankton growth consumes available nitrates (Goes et al., 2000). Conversely, exceedingly high chlorophyll levels significantly enhance the nitrate estimation, potentially signaling eutrophication events. Furthermore, during training, the model seemingly captures more valuable Chl-related information from alternative features such as CDM, redistributing Chl's overall contribution to 3D nitrate estimations.

As described above, the SHAP approach can explain the effect of each feature on the MLP output from both holistic and individual perspectives. This approach enables the comprehension of the role played by features in deep learning black box models. The ASV distribution of most features exhibits a long tail Fig. 13), suggesting that even features with low I_j can have a significant impact on model estimation in extreme environments. Nevertheless, the SHAP contribution is solely based on mathematical models and data-driven interpretations, which may result in conclusions that deviate physical processes. Although it has been experimentally validated that removing features with lower I_j results in less decline in model accuracy, the evaluation of the features still requires caution.

4 Conclusions

This study developed a continual learning-based MLP model tailored to estimate the 3D ocean nitrate concentration. The model was cross-validated by independent in situ data profiles and demonstrated satisfactory performance, achieving an R^2 of 0.98, RMSE of 0.592 $\mu mol \cdot kg^{-1}$ and MAE of 0.398 $\mu mol \cdot kg^{-1}$. It also exhibited robust and reliable performance in both site-based cross-validation and independent cruise observations. Contrasting experiments show that the model's generalization is notably enhanced by employing continual learning from simulated nitrate, especially in regions with limited data availability. The estimation accuracy remains general stable across all dimensions, with the more significant error occurring within the vertical range of 60-100 m and in the sparse region of the observations.

The 3D spatiotemporal distribution of nitrate is analyzed based on the reconstruction results. The findings indicate a progressive increase in oligotrophy from the western to eastern regions of the study area. Nitrate concentration shows significant seasonal variability in the vertical dimension, driven by seawater exchange and biological processes. From an interannual perspective, a discernible increase in nitrate concentrations was noted, especially since 2021. Besides, vertical consistency in

interannual anomalies within the NEA was lacking, with discrepancies commonly observed around depths of 100 m and 500 m.

The contribution of each feature is calculated to gain insight into their influence on nitrate estimation. Results reveal that spatial coordinates such as depth, longitude and environmental variables represented by SSH and SST exert the most significant influence. Meanwhile, certain features with low average contribution can still play vital roles in specific instances involving high anomalies.

The model still has certain limitations that require further improvements. Although its generalization ability has been enhanced, the nitrate distribution and trends in data-sparse regions should still be evaluated with caution. Due to the sparsity of BGC-Argo and the computational cost of CL, the model is limited to reconstructing water-column profiles without incorporating large-scale spatiotemporal global features, which may prevent it from fully leveraging the potential of deep learning models. The structure of the CL strategy imposes strict requirements on the datasets used for the two-stage training and may be affected by multiple sources of uncertainty, highlighting the need for higher-quality datasets in the future. Additionally, the current CL approach may introduce potential disturbances and performance fluctuations in regions with extensive BGC-Argo sampling. Future improvements could mitigate this limitation through dynamic weight parameters or additional modules.

From future perspectives, integrating remote sensing with deep learning for estimating oceanic 3D conditions holds significant research potential. Continual learning allows for the incorporation of numerical model knowledge to address the limitations of sparse in situ measurements and can be coupled with any deep learning model, making it a promising paradigm for reconstructing ocean datasets. Given the challenges of continuously high-resolution ocean monitoring, this approach can serve as an alternative solution to bridge the observation gap. Leveraging remote sensing expands retrieved variables and adds vertical dimension insights, supporting further research into marine environment.

Code availability.

All code used in the current study is available from the corresponding author upon reasonable request.

Data availability.

The reconstructed 3D nitrate concentration dataset presented in the paper can be accessed via Zenodo at https://doi.org/10.5281/zenodo.14010813 (Yu et al., 2024). Here we provide nitrate concentration gridded product for the pan-European ocean at $0.25° \times 0.25°$ horizontal resolution on 63 vertical levels from 0–2000 m and at a monthly resolution from 2010 to 2023.

Author contributions.

XY: Methodology, Data Curation, Software, Visualization, Writing - original draft. HG: Conceptualization, Funding acquisition, Supervision. JZ: Conceptualization, Funding acquisition, Supervision, Writing - review & editing. YM: Methodology, Supervision. XW: Formal analysis, Validation, Writing - review & editing. GL: Data curation, Validation, Writing - review & editing. MX: Formal analysis, Validation, Writing - review & editing. NX: Formal analysis, Validation, Writing - review & editing. AS: Formal analysis, Validation, Writing - review & editing. All authors have discussed the results and commented on the manuscript.

Competing interests.

The contact author has declared that none of the authors has any competing interests

Acknowledgements. The authors thank the International Argo Program, European Space Agency, European Centre for Medium-Range Weather Forecasts (ECMWF), Copernicus Climate Change Service, and GLODAPv2 for data, which are freely accessible for public. The BGC-Argo data were collected and made freely available by the International Argo Program and the national programs that contribute to it (https://argo.ucsd.edu, https://www.ocean-ops.org). The Argo Program is part of the Global Ocean Observing System. Biogeochemical data are from the European Copernicus Marine Environmental Monitoring Service (CMEMS, https://marine.copernicus.eu). The GlobColour data used in this study has been developed, validated, and distributed by ACRI-ST, France (http://globcolour.info). The ERA5 data are from the Copernicus Climate Change Service (https://cds.climate.copernicus.eu).

Financial support. The authors thank the anonymous reviewers whose comments and suggestions significantly improve this manuscript. This work was supported by the Strategic Priority Research Program of the Chinese Academy of Sciences-A (No. XDA19030402), Natural Science Foundation of China (No. 42071425), the "Taishan Scholar" Project of Shandong Province (No. TSXZ201712), and Discipline Cluster Research Project of Qingdao University "Deep mining and intelligent prediction of multimodal big data for marine ecological disasters" (No.XT2024101).

References

Akbari, E., Alavipanah, S., Jeihouni, M., Hajeb, M., Haase, D., and Alavipanah, S.: A Review of Ocean/Sea Subsurface Water Temperature Studies from Remote Sensing and Non-Remote Sensing Methods, Water, 9, 936, https://doi.org/10.3390/w9120936, 2017.

Ali, M. M., Swain, D., and Weller, R. A.: Estimation of Ocean Subsurface Thermal Structure from Surface Parameters: A Neural Network Approach, Geophys. Res. Lett., 31, 2004GL021 192, https://doi.org/10.1029/2004GL021192, 2004.

Altieri, K. E., Fawcett, S. E., Peters, A. J., Sigman, D. M., and Hastings, M. G.: Marine Biogenic Source of Atmospheric Organic Nitrogen in the Subtropical North Atlantic, PNAS, 113, 925–930, https://doi.org/10.1073/pnas.1516847113, 2016.

Altieri, K. E., Fawcett, S. E., and Hastings, M. G.: Reactive Nitrogen Cycling in the Atmosphere and Ocean, Annu. Rev. Earth Planet. Sci., 49, 523–550, https://doi.org/10.1146/annurev-earth-083120-052147, 2021.

Ansper, A. and Alikas, K.: Retrieval of Chlorophyll a from Sentinel-2 MSI Data for the European Union Water Framework Directive Reporting Purposes, Remote Sens., 11, 64, https://doi.org/10.3390/rs11010064, 2019.

Ascani, F., Richards, K. J., Firing, E., Grant, S., Johnson, K. S., Jia, Y., Lukas, R., and Karl, D. M.: Physical and Biological Controls of Nitrate Concentrations in the Upper Subtropical North Pacific Ocean, Deep Sea Res. Part II, 93, 119–134, https://doi.org/10.1016/j.dsr2.2013.01.034, 2013.

Asdar, S., Ciani, D., and Buongiorno Nardelli, B.: 3D Reconstruction of Horizontal and Vertical Quasi-Geostrophic Currents in the North Atlantic Ocean, Earth Syst. Sci. Data, 16, 1029–1046, https://doi.org/10.5194/essd-16-1029-2024, 2024.

Aumont, O., Éthé, C., Tagliabue, A., Bopp, L., and Gehlen, M.: PISCES-v2: An Ocean Biogeochemical Model for Carbon and Ecosystem Studies, Geosci. Model Dev. Discuss., 8, 1375–1509, 2015.

Baretta, J. W., Ebenhöh, W., and Ruardij, P.: The European Regional Seas Ecosystem Model, a Complex Marine Ecosystem Model, Neth. J. Sea Res., 33, 233–246, https://doi.org/10.1016/0077-7579(95)90047-0, 1995.

Ben-Ezra, T., Blachinsky, A., Gozali, S., Tsemel, A., Fadida, Y., Tchernov, D., Lehahn, Y., Tsagaraki, T. M., Berman-Frank, I., and Krom, M.: Interannual Changes in Nutrient and Phytoplankton Dynamics in the Eastern Mediterranean Sea (EMS) Predict the Consequences of Climate Change; Results from the Sdot-Yam Time-Series Station 2018-2022, https://doi.org/10.1101/2024.06.24.600321, 2024.

Berglund, S., Döös, K., Groeskamp, S., and McDougall, T.: North Atlantic Ocean Circulation and Related Exchange of Heat and Salt Between Water Masses, Geophys. Res. Lett., 50, e2022GL100 989, https://doi.org/10.1029/2022GL100989, 2023.

Bishop, C. M.: Neural Networks for Pattern Recognition., Oxford university press, ISBN 0-19-853864-2, 1995.

Bittig, H. C., Steinhoff, T., Claustre, H., Fiedler, B., Williams, N. L., Sauzède, R., Körtzinger, A., and Gattuso, J.-P.: An Alternative to Static Climatologies: Robust Estimation of Open Ocean CO2 Variables and Nutrient Concentrations from T, S, and O2 Data Using Bayesian Neural Networks, Front. Mar. Sci., 5, 328, https://doi.org/10.3389/fmars.2018.00328, 2018.

Bristow, L. A., Mohr, W., Ahmerkamp, S., and Kuypers, M. M.: Nutrients That Limit Growth in the Ocean, Curr. Biol., 27, R474–R478, https://doi.org/10.1016/j.cub.2017.03.030, 2017.

Bruggeman, J. and Bolding, K.: A General Framework for Aquatic Biogeochemical Models, Environ. Modell. Software, 61, 249–265, https://doi.org/10.1016/j.envsoft.2014.04.002, 2014.

Buongiorno Nardelli, B.: A Deep Learning Network to Retrieve Ocean Hydrographic Profiles from Combined Satellite and In Situ Measurements, Remote Sens., 12, 3151, 2020.

Cao, Z., Ma, R., Duan, H., Pahlevan, N., Melack, J., Shen, M., and Xue, K.: A Machine Learning Approach to Estimate Chlorophyll-a from Landsat-8 Measurements in Inland Lakes, Remote Sens. Environ., 248, 111 974, https://doi.org/10.1016/j.rse.2020.111974, 2020.

Chang, N.-B., Xuan, Z., and Yang, Y. J.: Exploring Spatiotemporal Patterns of Phosphorus Concentrations in a Coastal Bay with MODIS Images and Machine Learning Models, Remote Sens. Environ., 134, 100–110, https://doi.org/10.1016/j.rse.2013.03.002, 2013.

Chau, S. L., Hu, R., Gonzalez, J., and Sejdinovic, D.: RKHS-SHAP: Shapley Values for Kernel Methods, https://doi.org/10.48550/arXiv.2110.09167, 2022.

Chen, S., Hu, C., Barnes, B. B., Xie, Y., Lin, G., and Qiu, Z.: Improving Ocean Color Data Coverage through Machine Learning, Remote Sens. Environ., 222, 286–302, https://doi.org/10.1016/j.rse.2018.12.023, 2019.

Chen, S., Meng, Y., Lin, S., Yu, Y., and Xi, J.: Estimation of Sea Surface Nitrate from Space: Current Status and Future Potential, Sci. Total Environ., 899, 165 690, https://doi.org/10.1016/j.scitotenv.2023.165690, 2023.

Claustre, H., Johnson, K. S., and Takeshita, Y.: Observing the Global Ocean with Biogeochemical-Argo, Annu. Rev. Mar. Science, 12, 23–48, https://doi.org/10.1146/annurev-marine-010419-010956, 2020.

D'Ortenzio, F. and Ribera d'Alcalà, M.: On the Trophic Regimes of the Mediterranean Sea: A Satellite Analysis, Biogeosciences, 6, 139–148, https://doi.org/10.5194/bg-6-139-2009, 2009.

Du, C., Li, Y., Lyu, H., Liu, N., Zheng, Z., and Li, Y.: Remote Estimation of Total Phosphorus Concentration in the Taihu Lake Using a Semi-Analytical Model, Int. J. Remote Sens., 41, 7993–8013, https://doi.org/10.1080/01431161.2020.1767826, 2020.

Eppley, R. W. and Peterson, B. J.: Particulate Organic Matter Flux and Planktonic New Production in the Deep Ocean, Nature, 282, 677–680, https://doi.org/10.1038/282677a0, 1979.

Fisher, R. A. and Russell, E. J.: On the Mathematical Foundations of Theoretical Statistics, Philos. Trans. R. Soc. Lond., A, 222, 309–368, https://doi.org/10.1098/rsta.1922.0009, 1997.

Fourrier, M., Coppola, L., Claustre, H., D'Ortenzio, F., and Gattuso, J. P.: A Regional Neural Network Approach to Estimate Water-Column Nutrient Concentrations and Carbonate System Variables in the Mediterranean Sea: CANYON-MED, Front. Mar. Sci., 7, 620, https://doi.org/10.3389/fmars.2020.00620, 2020.

Fourrier, M., Coppola, L., D'Ortenzio, F., Migon, C., and Gattuso, J.-P.: Impact of Intermittent Convection in the Northwestern Mediterranean Sea on Oxygen Content, Nutrients, and the Carbonate System, J. Geophys. Res.: Oceans, 127, e2022JC018 615, https://doi.org/10.1029/2022JC018615, 2022.

Friedlingstein, P., O'sullivan, M., Jones, M. W., Andrew, R. M., Hauck, J., Olsen, A., Peters, G. P., Peters, W., Pongratz, J., and Sitch, S.: Global Carbon Budget 2020, Earth Syst. Sci. Data, 12, 3269–3340, https://doi.org/10.5194/essd-12-3269-2020, 2020.

Fripiat, F., Martínez-García, A., Marconi, D., Fawcett, S. E., Kopf, S. H., Luu, V. H., Rafter, P. A., Zhang, R., Sigman, D. M., and Haug, G. H.: Nitrogen Isotopic Constraints on Nutrient Transport to the Upper Ocean, Nat. Geosci., 14, 855–861, https://doi.org/10.1038/s41561-021-00836-8, 2021.

Gao, H., Huang, B., Chen, G., Xia, L., and Radenkovic, M.: Deep Learning Solver Unites SDGSAT-1 Observations and Navier–Stokes Theory for Oceanic Vortex Streets, Remote Sensing of Environment, 315, 114 425, https://doi.org/10.1016/j.rse.2024.114425, 2024.

Gattuso, J.-P., Frankignoulle, M., Wollast, R., and Systematics: Carbon and Carbonate Metabolism in Coastal Aquatic Ecosystems, Annu. Rev. Ecol., 29, 405–434, https://doi.org/10.1146/annurev.ecolsys.29.1.405, 1998.

Goes, J. I., Saino, T., Oaku, H., and Jiang, D. L.: A Method for Estimating Sea Surface Nitrate Concentrations from Remotely Sensed SST and Chlorophyll Aa Case Study for the North Pacific Ocean Using OCTS/ADEOS Data, IEEE Trans. Geosci. Remote Sens., 37, 1633–1644, https://doi.org/10.1109/36.763279, 1999.

Goes, J. I., Saino, T., Oaku, H., Ishizaka, J., Wong, C. S., and Nojiri, Y.: Basin Scale Estimates of Sea Surface Nitrate and New Production from Remotely Sensed Sea Surface Temperature and Chlorophyll, Geophys. Res. Lett., 27, 1263–1266, https://doi.org/10.1029/1999GL002353, 2000.

Gregg, W. W., Conkright, M. E., Ginoux, P., O'Reilly, J. E., and Casey, N. W.: Ocean Primary Production and Climate: Global Decadal Changes, Geophys. Res. Lett., 30, 1089, https://doi.org/10.1029/2003GL016889, 2003.

Hagan, M. T., Demuth, H. B., and Beale, M.: Neural Network Design, PWS Publishing Co., ISBN 0-534-94332-2, 1997.

Harkort, L. and Duan, Z.: Estimation of Dissolved Organic Carbon from Inland Waters at a Large Scale Using Satellite Data and Machine Learning Methods, Water Res., 229, 119 478, https://doi.org/10.1016/j.watres.2022.119478, 2023.

Hersbach, H., Bell, B., Berrisford, P., Hirahara, S., Horányi, A., Muñoz-Sabater, J., Nicolas, J., Peubey, C., Radu, R., and Schepers, D.: The ERA5 Global Reanalysis, Q. J. R. Meteorolog. Soc., 146, 1999–2049, https://doi.org/10.1002/qj.3803, 2020.

Holt, J., Harle, J., Proctor, R., Michel, S., Ashworth, M., Batstone, C., Allen, I., Holmes, R., Smyth, T., and Haines, K.: Modelling the Global Coastal Ocean, Philos. T. Roy. Soc. A., 367, 939–951, https://doi.org/10.1098/rsta.2008.0210, 2009.

Holt, J., Butenschön, M., Wakelin, S. L., Artioli, Y., and Allen, J. I.: Oceanic Controls on the Primary Production of the Northwest European Continental Shelf: Model Experiments under Recent Past Conditions and a Potential Future Scenario, Biogeosciences, 9, 97–117, https://doi.org/10.5194/bg-9-97-2012, 2012.

Hu, Q., Chen, X., Bai, Y., He, X., Li, T., and Pan, D.: Reconstruction of 3-D Ocean Chlorophyll a Structure in the Northern Indian Ocean Using Satellite and BGC-Argo Data, IEEE Trans. Geosci. Remote Sens., 61, 1–13, https://doi.org/10.1109/TGRS.2022.3233385, 2023.

Huang, J., Wang, D., Gong, F., Bai, Y., and He, X.: Changes in Nutrient Concentrations in Shenzhen Bay Detected Using Landsat Imagery between 1988 and 2020, Remote Sens., 13, 3469, https://doi.org/10.3390/rs13173469, 2021.

Hutchins, D. A. and Capone, D. G.: The Marine Nitrogen Cycle: New Developments and Global Change, Nat. Rev. Microbiol., 20, 401–414, https://doi.org/10.1038/s41579-022-00687-z, 2022.

Johnson, K., Maurer, T., Plant, J., Bittig, H., Schallenberg, C., and Schmechtig, C.: BGC-Argo Quality Control Manual for Nitrate Concentration., https://doi.org/10.13155/84370, 2021.

Johnson, K. S., Plant, J. N., Coletti, L. J., Jannasch, H. W., Sakamoto, C. M., Riser, S. C., Swift, D. D., Williams, N. L., Boss, E., Haëntjens, N., Talley, L. D., and Sarmiento, J. L.: Biogeochemical Sensor Performance in the SOCCOM Profiling Float Array, J. Geophys. Res.: Oceans, 122, 6416–6436, https://doi.org/10.1002/2017JC012838, 2017.

Johnson, K. S., Plant, J. N., Sakamoto, C., Maurer, T. L., Pasqueron De Fommervault, O., Serra, R., D'Ortenzio, F., Schmechtig, C., Claustre, H., and Poteau, A.: Processing BGC-Argo Nitrate Concentration at the DAC Level, https://doi.org/10.13155/46121, 2024.

Joo, H., Son, S., Park, J.-W., Kang, J. J., Jeong, J.-Y., Lee, C. I., Kang, C.-K., and Lee, S. H.: Long-Term Pattern of Primary Productivity in the East/Japan Sea Based on Ocean Color Data Derived from MODIS-aqua, Remote Sens., 8, 25, https://doi.org/10.3390/rs8010025, 2016.

Joo, H., Lee, D., Kang, J. J., Lee, J. H., Jeong, J.-Y., Son, S.-H., Kwon, J.-I., and Lee, S. H.: Inter-Annual Variation of the Annual New Production of Phytoplankton in the Southwestern East/Japan Sea Estimated from Satellite-Derived Surface Nitrate Concentration, J. Coastal Res., pp. 336–340, https://doi.org/10.2112/SI85-068.1, 2018.

Kamykowski, D., Zentara, S.-J., Morrison, J. M., and Switzer, A. C.: Dynamic Global Patterns of Nitrate, Phosphate, Silicate, and Iron Availability and Phytoplankton Community Composition from Remote Sensing Data, Global Biogeochem. Cycles, 16, 25–1–25–29, https://doi.org/10.1029/2001GB001640, 2002.

Kay, S. and Butenschön, M.: Projections of Change in Key Ecosystem Indicators for Planning and Management of Marine Protected Areas: An Example Study for European Seas, Estuarine Coastal Shelf Sci., 201, 172–184, https://doi.org/10.1016/j.ecss.2016.03.003, 2018.

Kirkpatrick, J., Pascanu, R., Rabinowitz, N., Veness, J., Desjardins, G., Rusu, A. A., Milan, K., Quan, J., Ramalho, T., Grabska-Barwinska, A., Hassabis, D., Clopath, C., Kumaran, D., and Hadsell, R.: Overcoming Catastrophic Forgetting in Neural Networks, PNAS, 114, 3521–3526, https://doi.org/10.1073/pnas.1611835114, 2017.

Kudela, R. M. and Dugdale, R. C.: Nutrient Regulation of Phytoplankton Productivity in Monterey Bay, California, Deep Sea Res. Part II, 47, 1023–1053, https://doi.org/10.1016/S0967-0645(99)00135-6, 2000.

Lauvset, S. K., Lange, N., Tanhua, T., Bittig, H. C., Olsen, A., Kozyr, A., Álvarez, M., Becker, S., Brown, P. J., Carter, B. R., Cotrim Da Cunha, L., Feely, R. A., Van Heuven, S., Hoppema, M., Ishii, M., Jeansson, E., Jutterström, S., Jones, S. D., Karlsen, M. K., Lo Monaco, C., Michaelis, P., Murata, A., Pérez, F. F., Pfeil, B., Schirnick, C., Steinfeldt, R., Suzuki, T., Tilbrook, B., Velo, A., Wanninkhof, R., Woosley, R. J., and Key, R. M.: An Updated Version of the Global Interior Ocean Biogeochemical Data Product, GLODAPv2.2021, Earth Syst. Sci. Data, 13, 5565–5589, https://doi.org/10.5194/essd-13-5565-2021, 2021.

Lauvset, S. K., Lange, N., Tanhua, T., Bittig, H. C., Olsen, A., Kozyr, A., Alin, S., Álvarez, M., Azetsu-Scott, K., Barbero, L., Becker, S., Brown, P. J., Carter, B. R., Da Cunha, L. C., Feely, R. A., Hoppema, M., Humphreys, M. P., Ishii, M., Jeansson, E., Jiang, L.-Q., Jones, S. D., Lo Monaco, C., Murata, A., Müller, J. D., Pérez, F. F., Pfeil, B., Schirnick, C., Steinfeldt, R., Suzuki, T., Tilbrook, B., Ulfsbo, A., Velo, A., Woosley, R. J., and Key, R. M.: GLODAPv2.2022: The Latest Version of the Global Interior Ocean Biogeochemical Data Product, Earth Syst. Sci. Data, 14, 5543–5572, https://doi.org/10.5194/essd-14-5543-2022, 2022.

Lavender, S., Antoine, D., Maritorena, S., Morel, A., Barrot, G., Demaria, J., and Pinnock, S.: GlobColour—The European Service for Ocean Colour, in: Proceedings of the 2009 IEEE International Geoscience & Remote Sensing Symposium, Cape Town, South Africa, pp. 12–17, 2009.

Lavigne, H., D'ortenzio, F., Ribera D'Alcalà, M., Claustre, H., Sauzède, R., and Gacic, M.: On the Vertical Distribution of the Chlorophyll a Concentration in the Mediterranean Sea: A Basin-Scale and Seasonal Approach, Biogeosciences, 12, 5021–5039, https://doi.org/10.5194/bgd-12-4139-2015, 2015.

Liu, Y., Tang, D., and Evgeny, M.: Chlorophyll Concentration Response to the Typhoon Wind-Pump Induced Upper Ocean Processes Considering Air–Sea Heat Exchange, Remote Sens., 11, 1825, https://doi.org/10.3390/rs11151825, 2019.

Longhurst, A., Sathyendranath, S., Platt, T., and Caverhill, C.: An Estimate of Global Primary Production in the Ocean from Satellite Radiometer Data, J. Plankton Res., 17, 1245–1271, https://doi.org/10.1093/plankt/17.6.1245, 1995.

Lundberg, S. M. and Lee, S.-I.: A Unified Approach to Interpreting Model Predictions, in: Proceedings of the 31st International Conference on Neural Information Processing Systems, pp. 4768–4777, 2017.

Lv, Q., Wang, D., Gong, F., Bai, Y., and He, X.: Nitrate Inversion Based on Remote Sensing in the Pearl River Estuary, China, in: IOP Conference Series: Earth and Environmental Science, vol. 502, p. 012027, IOP Publishing, ISBN 1755-1315, https://doi.org/10.1088/1755-1315/502/1/012027, 2020.

Ma, Y., Chen, S., Ermon, S., and Lobell, D. B.: Transfer Learning in Environmental Remote Sensing, Remote Sens. Environ., 301, 113 924, https://doi.org/10.1016/j.rse.2023.113924, 2024.

MacKay, D. J. C.: Bayesian Interpolation, Neural Comput., 4, 415–447, https://doi.org/10.1162/neco.1992.4.3.415, 1992.

Macovei, V. A., Torres-Valdés, S., Hartman, S. E., Schuster, U., Moore, C. M., Brown, P. J., Hydes, D. J., and Sanders, R. J.: Temporal Variability in the Nutrient Biogeochemistry of the Surface North Atlantic: 15 Years of Ship of Opportunity Data, Global Biogeochemical Cycles, 33, 1674–1692, https://doi.org/10.1029/2018GB006132, 2019.

Madec, G.: NEMO Reference Manual 3_6_STABLE: NEMO Ocean Engine, Note du Pôle modél. Inst. Pierre-Simon Laplace (IPSL) Fr., 2016.

Miao, Y., Zhang, X., Li, Y., Zhang, L., and Zhang, D.: Monthly Extended Ocean Predictions Based on a Convolutional Neural Network via the Transfer Learning Method, Front. Mar. Sci., 9, 1073 377, https://doi.org/10.3389/fmars.2022.1073377, 2023.

Mignot, A., D'Ortenzio, F., Taillandier, V., Cossarini, G., and Salon, S.: Quantifying Observational Errors in Biogeochemical-Argo Oxygen, Nitrate, and Chlorophyll *a* Concentrations, Geophys. Res. Lett., 46, 4330–4337, https://doi.org/10.1029/2018GL080541, 2019.

Moore, C. M., Mills, M. M., Arrigo, K. R., Berman-Frank, I., Bopp, L., Boyd, P. W., Galbraith, E. D., Geider, R. J., Guieu, C., and Jaccard, S. L.: Processes and Patterns of Oceanic Nutrient Limitation, Nature geoscience, 6, 701–710, https://doi.org/10.1038/ngeo1765, 2013.

Morel, A. and Berthon, J.-F.: Surface Pigments, Algal Biomass Profiles, and Potential Production of the Euphotic Layer: Relationships Reinvestigated in View of Remote-sensing Applications, Limnol. Oceanogr., 34, 1545–1562, https://doi.org/10.2307/2837038, 1989.

Mortula, M., Ali, T., Bachir, A., Elaksher, A., and Abouleish, M.: Towards Monitoring of Nutrient Pollution in Coastal Lake Using Remote Sensing and Regression Analysis, Water, 12, 1954, https://doi.org/10.3390/w12071954, 2020.

Nittis, K., Tziavos, C., Bozzano, R., Cardin, V., Thanos, Y., Petihakis, G., Schiano, M. E., and Zanon, F.: The M3A Multi-Sensor Buoy Network of the Mediterranean Sea, Ocean Sci., 3, 229–243, https://doi.org/10.5194/os-3-229-2007, 2007.

Olsen, A., Lange, N., Key, R. M., Tanhua, T., Bittig, H. C., Kozyr, A., Álvarez, M., Azetsu-Scott, K., Becker, S., Brown, P. J., Carter, B. R., Cotrim Da Cunha, L., Feely, R. A., Van Heuven, S., Hoppema, M., Ishii, M., Jeansson, E., Jutterström, S., Landa, C. S., Lauvset, S. K., Michaelis, P., Murata, A., Pérez, F. F., Pfeil, B., Schirnick, C., Steinfeldt, R., Suzuki, T., Tilbrook, B., Velo, A., Wanninkhof, R., and Woosley, R. J.: An Updated Version of the Global Interior Ocean Biogeochemical Data Product, GLODAPv2.2020, Earth Syst. Sci. Data, 12, 3653–3678, https://doi.org/10.5194/essd-12-3653-2020, 2020.

Padin, X. A., Velo, A., and Pérez, F. F.: ARIOS: A Database for Ocean Acidification Assessment in the Iberian Upwelling System (1976–2018), Earth System Science Data, 12, 2647–2663, https://doi.org/10.5194/essd-12-2647-2020, 2020.

Pan, X., Wong, G. T., Ho, T.-Y., Tai, J.-H., Liu, H., Liu, J., and Shiah, F.-K.: Remote Sensing of Surface [Nitrite+ Nitrate] in River-Influenced Shelf-Seas: The Northern South China Sea Shelf-sea, Remote Sens. Environ., 210, 1–11, https://doi.org/10.1016/j.rse.2018.03.012, 2018.

Pauthenet, E., Bachelot, L., Balem, K., Maze, G., Tréguier, A.-M., Roquet, F., Fablet, R., and Tandeo, P.: Four-Dimensional Temperature, Salinity and Mixed-Layer Depth in the Gulf Stream, Reconstructed from Remote-Sensing and in Situ Observations with Neural Networks, Ocean Sci., 18, 1221–1244, https://doi.org/10.5194/os-18-1221-2022, 2022.

Pujo-Pay, M., Conan, P., Oriol, L., Cornet-Barthaux, V., Falco, C., Ghiglione, J.-F., Goyet, C., Moutin, T., and Prieur, L.: Integrated Survey of Elemental Stoichiometry (C, N, P) from the Western to Eastern Mediterranean Sea, Biogeosciences, 8, 883–899, https://doi.org/10.5194/bg-8-883-2011, 2011.

Qi, J., Liu, C., Chi, J., Li, D., Gao, L., and Yin, B.: An Ensemble-Based Machine Learning Model for Estimation of Subsurface Thermal Structure in the South China Sea, Remote Sens., 14, 3207, https://doi.org/10.3390/rs14133207, 2022.

Qun'ou, J., Lidan, X., Siyang, S., Meilin, W., and Huijie, X.: Retrieval Model for Total Nitrogen Concentration Based on UAV Hyper Spectral Remote Sensing Data and Machine Learning Algorithms–A Case Study in the Miyun Reservoir, China, Ecol. Indic., 124, 107 356, https://doi.org/10.1016/j.ecolind.2021.107356, 2021.

Rafter, P. A., Sigman, D. M., and Mackey, K. R.: Recycled Iron Fuels New Production in the Eastern Equatorial Pacific Ocean, Nat. Commun., 8, 1–10, https://doi.org/10.1038/s41467-017-01219-7, 2017.

Reale, M., Cossarini, G., Lazzari, P., Lovato, T., Bolzon, G., Masina, S., Solidoro, C., and Salon, S.: Acidification, Deoxygenation, and Nutrient and Biomass Declines in a Warming Mediterranean Sea, Biogeosciences, 19, 4035–4065, https://doi.org/10.5194/bg-19-4035-2022, 2022.

Ribera d'Alcalà, M., Civitarese, G., Conversano, F., and Lavezza, R.: Nutrient Ratios and Fluxes Hint at Overlooked Processes in the Mediterranean Sea, J. Geophys. Res.: Oceans, 108, 8106, https://doi.org/10.1029/2002JC001650, 2003.

Richardson, A. J., Pfaff, M. C., Field, J. G., Silulwane, N. F., and Shillington, F. A.: Identifying Characteristic Chlorophyll a Profiles in the Coastal Domain Using an Artificial Neural Network, J. Plankton Res., 24, 1289–1303, https://doi.org/10.1093/plankt/24.12.1289, 2002.

Rossi, P., Ponti, M., Righi, S., Castagnetti, C., Simonini, R., Mancini, F., Agrafiotis, P., Bassani, L., Bruno, F., Cerrano, C., Cignoni, P., Corsini, M., Drap, P., Dubbini, M., Garrabou, J., Gori, A., Gracias, N., Ledoux, J.-B., Linares, C., Mantas, T. P., Menna, F., Nocerino, E., Palma, M., Pavoni, G., Ridolfi, A., Rossi, S., Skarlatos, D., Treibitz, T., Turicchia, E., Yuval, M., and Capra, A.: Needs and Gaps in Optical Underwater Technologies and Methods for the Investigation of Marine Animal Forest 3D-Structural Complexity, Front. Mar. Sci., 8, 591 292, https://doi.org/10.3389/fmars.2021.591292, 2021.

Rumelhart, D. E., Hinton, G. E., and Williams, R. J.: Learning Representations by Back-Propagating Errors, Nature, 323, 533–536, https://doi.org/10.1038/323533a0, 1986.

Salazar, J. J., Garland, L., Ochoa, J., and Pyrcz, M. J.: Fair Train-Test Split in Machine Learning: Mitigating Spatial Autocorrelation for Improved Prediction Accuracy, J. Pet. Sci. Eng., 209, 109 885, https://doi.org/10.1016/j.petrol.2021.109885, 2022.

Sammartino, M., Nardelli, B., Marullo, S., and Santoleri, R.: An Artificial Neural Network to Infer the Mediterranean 3D Chlorophyll-a and Temperature Fields from Remote Sensing Observations, Remote Sens., 12, 4123, https://doi.org/10.3390/rs12244123, 2020.

Sarangi, R. and Devi, K. N.: Space-Based Observation of Chlorophyll, Sea Surface Temperature, Nitrate, and Sea Surface Height Anomaly over the Bay of Bengal and Arabian Sea, Adv. Space Res., 59, 33–44, https://doi.org/10.1016/j.asr.2016.08.038, 2017.

Sathyendranath, S., Platt, T., Horne, E. P., Harrison, W. G., Ulloa, O., Outerbridge, R., and Hoepffner, N.: Estimation of New Production in the Ocean by Compound Remote Sensing, Nature, 353, 129–133, https://doi.org/10.1038/353129a0, 1991.

Sauzède, R., Bittig, H. C., Claustre, H., Pasqueron de Fommervault, O., Gattuso, J.-P., Legendre, L., and Johnson, K. S.: Estimates of Water-Column Nutrient Concentrations and Carbonate System Parameters in the Global Ocean: A Novel Approach Based on Neural Networks, Front. Mar. Sci., 4, 128, https://doi.org/10.3389/fmars.2017.00128, 2017.

Severin, T., Kessouri, F., Rembauville, M., Sánchez-Pérez, E. D., Oriol, L., Caparros, J., Pujo-Pay, M., Ghiglione, J.-F., D'Ortenzio, F., Taillandier, V., Mayot, N., Durrieu De Madron, X., Ulses, C., Estournel, C., and Conan, P.: Open-ocean Convection Process: A Driver of the Winter Nutrient Supply and the Spring Phytoplankton Distribution in the N Orthwestern M Editerranean S Ea, Journal of Geophysical Research: Oceans, 122, 4587–4601, https://doi.org/10.1002/2016JC012664, 2017.

Shapley, L. S.: A Value for N-Person Games, The Shapley Value: Essays in Honor of Lloyd S. Shapley, Cambridge University Press, Cambridge, ISBN 978-0-521-36177-4, 1988.

Silió-Calzada, A., Bricaud, A., and Gentili, B.: Estimates of Sea Surface Nitrate Concentrations from Sea Surface Temperature and Chlorophyll Concentration in Upwelling Areas: A Case Study for the Benguela System, Remote Sens. Environ., 112, 3173–3180, https://doi.org/10.1016/j.rse.2008.03.014, 2008.

Smith, P. A. H., Sørensen, K. A., Buongiorno Nardelli, B., Chauhan, A., Christensen, A., St. John, M., Rodrigues, F., and Mariani, P.: Reconstruction of Subsurface Ocean State Variables Using Convolutional Neural Networks with Combined Satellite and in Situ Data, Front. Mar. Sci., 10, 1218 514, https://doi.org/10.3389/fmars.2023.1218514, 2023.

Smith, S. V. and Hollibaugh, J. T.: Coastal Metabolism and the Oceanic Organic Carbon Balance, Rev. Geophys., 31, 75–89, https://doi.org/10.1029/92rg02584, 1993.

Stéphane, Maritorena, Odile, Hembise, F anton, d 'Andon, Antoine, Mangin, David, and A: Merged Satellite Ocean Color Data Products Using a Bio-Optical Model: Characteristics, Benefits and Issues, Remote Sens. Environ., 114, 1791–1804, https://doi.org/10.1016/j.rse.2010.04.002, 2010.

Storto, A., Alvera-Azcárate, A., Balmaseda, M. A., Barth, A., Chevallier, M., Counillon, F., Domingues, C. M., Drevillon, M., Drillet, Y., Forget, G., Garric, G., Haines, K., Hernandez, F., Iovino, D., Jackson, L. C., Lellouche, J.-M., Masina, S., Mayer, M., Oke, P. R., Penny, S. G., Peterson, K. A., Yang, C., and Zuo, H.: Ocean Reanalyses: Recent Advances and Unsolved Challenges, Front. Mar. Sci., 6, 418, https://doi.org/10.3389/fmars.2019.00418, 2019.

Su, H., Zhang, T., Lin, M., Lu, W., and Yan, X.-H.: Predicting Subsurface Thermohaline Structure from Remote Sensing Data Based on Long Short-Term Memory Neural Networks, Remote Sens. Environ., 260, 112 465, https://doi.org/10.1016/j.rse.2021.112465, 2021.

Su, H., Qiu, J., Tang, Z., Huang, Z., and Yan, X.-H.: Retrieving Global Ocean Subsurface Density by Combining Remote Sensing Observations and Multiscale Mixed Residual Transformer, IEEE Trans. Geosci. Remote Sens., 62, 1–13, https://doi.org/10.1109/TGRS.2024.3350346, 2024.

Switzer, A. C., Kamykowski, D., and Zentara, S.-J.: Mapping Nitrate in the Global Ocean Using Remotely Sensed Sea Surface Temperature, J. Geophys. Res.: Oceans, 108, 2000JC000 444, https://doi.org/10.1029/2000JC000444, 2003.

Syariz, M. A., Lin, C.-H., Nguyen, M. V., Jaelani, L. M., and Blanco, A. C.: WaterNet: A Convolutional Neural Network for Chlorophyll-a Concentration Retrieval, Remote Sens., 12, https://doi.org/10.3390/rs12121966, 2020.

Tian, T., Cheng, L., Wang, G., Abraham, J., Wei, W., Ren, S., Zhu, J., Song, J., and Leng, H.: Reconstructing Ocean Subsurface Salinity at High Resolution Using a Machine Learning Approach, Earth Syst. Sci. Data, 14, 5037–5060, https://doi.org/10.5194/essd-14-5037-2022, 2022.

Tuerena, R. E., Williams, R. G., Mahaffey, C., Vic, C., Green, J. M., Naveira-Garabato, A., Forryan, A., and Sharples, J.: Internal Tides Drive Nutrient Fluxes into the Deep Chlorophyll Maximum over Mid-ocean Ridges, Global Biogeochem. Cycles, 33, 995–1009, https://doi.org/10.1029/2019gb006214, 2019.

Uitz, J., Claustre, H., Morel, A., and Hooker, S. B.: Vertical Distribution of Phytoplankton Communities in Open Ocean: An Assessment Based on Surface Chlorophyll, J. Geophys. Res.: Oceans, 111, C08 005, https://doi.org/10.1029/2005JC003207, 2006.

Von Schuckmann, K., Le Traon, P.-Y., Smith, N., Pascual, A., Djavidnia, S., Gattuso, J.-P., Grégoire, M., Nolan, G., Aaboe, S., and Aguiar, E.: Copernicus Marine Service Ocean State Report, Issue 3, J. Oper. Oceanogr., 12, S1–S123, https://doi.org/10.1080/1755876X.2019.1633075, 2019.

Wang, L., Xu, Z., Gong, X., Zhang, P., Hao, Z., You, J., Zhao, X., and Guo, X.: Estimation of Nitrate Concentration and Its Distribution in the Northwestern Pacific Ocean by a Deep Neural Network Model, Deep Sea Res. Part I, 195, 104 005, https://doi.org/10.1016/j.dsr.2023.104005, 2023.

Wang, T., Chai, F., Xing, X., Ning, J., Jiang, W., and Riser, S. C.: Influence of Multi-Scale Dynamics on the Vertical Nitrate Distribution around the Kuroshio Extension: An Investigation Based on BGC-Argo and Satellite Data, Prog. Oceanogr., 193, 102 543, https://doi.org/10.1016/j.pocean.2021.102543, 2021.

Webb, P.: Introduction to Oceanography, Roger Williams University, 2021.

Yang, G. G., Wang, Q., Feng, J., He, L., Li, R., Lu, W., Liao, E., and Lai, Z.: Can Three-Dimensional Nitrate Structure Be Reconstructed from Surface Information with Artificial Intelligence? — a Proof-of-Concept Study, Science of the Total Environment, 924, 171 365, https://doi.org/10.1016/j.scitotenv.2024.171365, 2024.

Yu, X., Yi, H., Liu, X., Wang, Y., Liu, X., and Zhang, H.: Remote-Sensing Estimation of Dissolved Inorganic Nitrogen Concentration in the Bohai Sea Using Band Combinations Derived from MODIS Data, Int. J. Remote Sens., 37, 327–340, https://doi.org/10.1080/01431161.2015.1125555, 2016.

Yu, X., Chen, S., and Chai, F.: Remote Estimation of Sea Surface Nitrate in the California Current System From Satellite Ocean Color Measurements, IEEE Transactions on Geoscience and Remote Sensing, 60, 1–17, https://doi.org/10.1109/TGRS.2021.3095099, 2022.

Yu, X., Guo, H., Zhang, J., Ma, Y., Wang, X., Liu, G., Xing, M., Xu, N., and Seka, A. M.: The Reconstructed Three-Dimensional Nitrate Field Dataset for the Pan-European Ocean Using a Continual Learning-Based Multilayer Perceptron, Zenodo [dataset], https://doi.org/10.5281/zenodo.14010813, 2024.

Zakem, E. J., Al-Haj, A., Church, M. J., Van Dijken, G. L., Dutkiewicz, S., Foster, S. Q., Fulweiler, R. W., Mills, M. M., and Follows, M. J.: Ecological Control of Nitrite in the Upper Ocean, Nat. Commun., 9, 1206, https://doi.org/10.1038/s41467-018-03553-w, 2018.

Zhou, L. and Zhang, R.-H.: A Self-Attention–Based Neural Network for Three-Dimensional Multivariate Modeling and Its Skillful ENSO Predictions, Science Advances, 9, eadf2827, https://doi.org/10.1126/sciadv.adf2827, 2023.

Zhu, X. X., Tuia, D., Mou, L., Xia, G.-S., Zhang, L., Xu, F., and Fraundorfer, F.: Deep Learning in Remote Sensing: A Comprehensive Review and List of Resources, IEEE Geosci. Remote Sens. Mag., 5, 8–36, https://doi.org/10.1109/MGRS.2017.2762307, 2017.